

Metallurgical Investigation into Ductility Dip Cracking in Ni-Based Alloys: Part II

Microstructural and microchemical development is characterized during simulated weld reheat thermal cycle and correlated to ductility dip cracking susceptibility

BY F. F. NOECKER II AND J. N. DUPONT

ABSTRACT

In this second of two papers, the microstructural and microchemical evolution of Alloy 600 (A600), Alloy 690 (A690), Filler Metal 82H (FM82H), and Filler Metal 52 (FM52) during the weld thermal cycle was investigated and compared to the hot ductility data presented in the first paper (Ref. 1). The Gleeble® hot ductility test was used to subject these four alloys to a simulated weld thermal cycle. Water quenching was conducted at select temperatures so that the elevated temperature microstructure could be subsequently characterized. Microstructural and microchemical characterization was carried out using scanning electron microscopy, transmission electron microscopy, and analytical electron microscopy techniques. Complete dissolution of intergranular carbides was observed in A690 and FM52 at ~2400°F (1316°C), both of which exhibit an on-cooling ductility minimum at 1600°F (871°C). Of all four alloys, the greatest resistance to ductility dip cracking (DDC) was observed in A600 and A690 during on-heating, which had coarse, homogeneously distributed intergranular carbides. FM82H, which formed NbC intergranular carbides, had the most stable intergranular microstructure and serrated grain boundaries, which corresponded to the best overall DDC resistance. Modifications to the thermal cycle that resulted in increased intergranular carbide coverage in FM82H and FM52 also reduced DDC susceptibility. AEM analysis did not

reveal any sulfur or phosphorous segregation in FM52 at 1600°F (871°C) on-heating, on-cooling, or after a 60-s hold. Samples with microstructures that consisted of coarsened carbides and/or serrated grain boundaries, which are expected to decrease grain boundary sliding, were found to be resistant to DDC. Based on the results of this work and the results previously presented in Paper I (Ref. 1), grain boundary sliding contributes to DDC. Conversely, sulfur and phosphorous embrittlement do not play a role in DDC of FM52 at the concentrations investigated. The dynamic precipitation of partially coherent intergranular $M_{23}C_6$ carbides at intermediate temperatures may exacerbate DDC in A690 and FM52, but requires further investigation.

Introduction

In the first paper of this two part series the Gleeble® hot ductility test was used to evaluate the DDC susceptibility of wrought A600 and A690, along with their companion filler metals, FM82H and FM52, throughout the heating and cooling portions of a simulated weld thermal cycle. Both macroscopic mechanical measures (ductility and ultimate tensile strength (UTS)), and microscopic measures (normalized crack length) of DDC were quantified and compared. The macroscopic measures of DDC were found to have reasonable agreement with normalized crack

length. The hot ductility curves for all four alloys are presented in Fig. 1.

Of all four alloys, the greatest resistance to DDC was observed in A600 and A690 during heating, where no ductility dip cracks formed even when the samples were strained to fracture. Both A690 and FM52 were found to form an intermediate on-cooling dip in ductility and ultimate tensile strength (UTS), which corresponded to an increase in the amount of intergranular ductility dip crack length normalized per grain boundary length. The normalized crack length decreased in both FM52 and FM82H when the thermal cycle was modified to promote precipitation/coarsening of intergranular carbides. The precipitation/coarsening of intergranular carbides can act to decrease grain boundary sliding (GBS), and may also act by reducing strain at the partially coherent $M_{23}C_6$ precipitate/matrix interface by decreasing lattice/precipitate misfit. In these tests FM82H has the best overall (on-heating and on-cooling) resistance to DDC due to its serrated grain boundaries and presence of MC-type grain boundary carbides, which are very effective at reducing DDC susceptibility.

Recently, a significant amount of research has been performed to identify the mechanism(s) of DDC. There are three prevailing hypotheses that will be briefly reviewed: impurity element (sulfur and phosphorous) embrittlement, precipitation-induced cracking, and grain boundary sliding. Grain boundary sliding (GBS) was first proposed by Rhines and Wray based on their observations of tensile deformation behavior at intermediate temperatures in brass, 70%Ni-30%Cu, and Monel (Ref. 2). Typical time to fracture during their testing was approximately 10 s. They proposed that DDC was a creep-like phenomena, where the ductility decreases with decreasing strain rate (Ref. 2). This strain rate sensitivity was also seen in Invar, where GBS increased with decreasing stroke rate at intermediate temperatures, which resulted in a larger intermediate temperature ductility dip (Ref. 3). Decreasing strain rate has also been

KEYWORDS

Alloy 600 (A600)
Alloy 690 (A690)
Filler Metal 82H (FM82H)
Filler Metal 52 (FM52)
Gleeble® Hot Ductility Test
Water Quenched
Ductility Dip Cracking (DDC)

F. F. NOECKER II (ffn2us@yahoo.com), formerly a research assistant, Department of Materials Science and Engineering, Lehigh University, Bethlehem, Pa., is currently a materials specialist, ExxonMobil, Upstream Development Co., Houston, Tex. J. N. DUPONT is a professor, Department of Materials Science and Engineering, Lehigh University, Bethlehem, Pa.

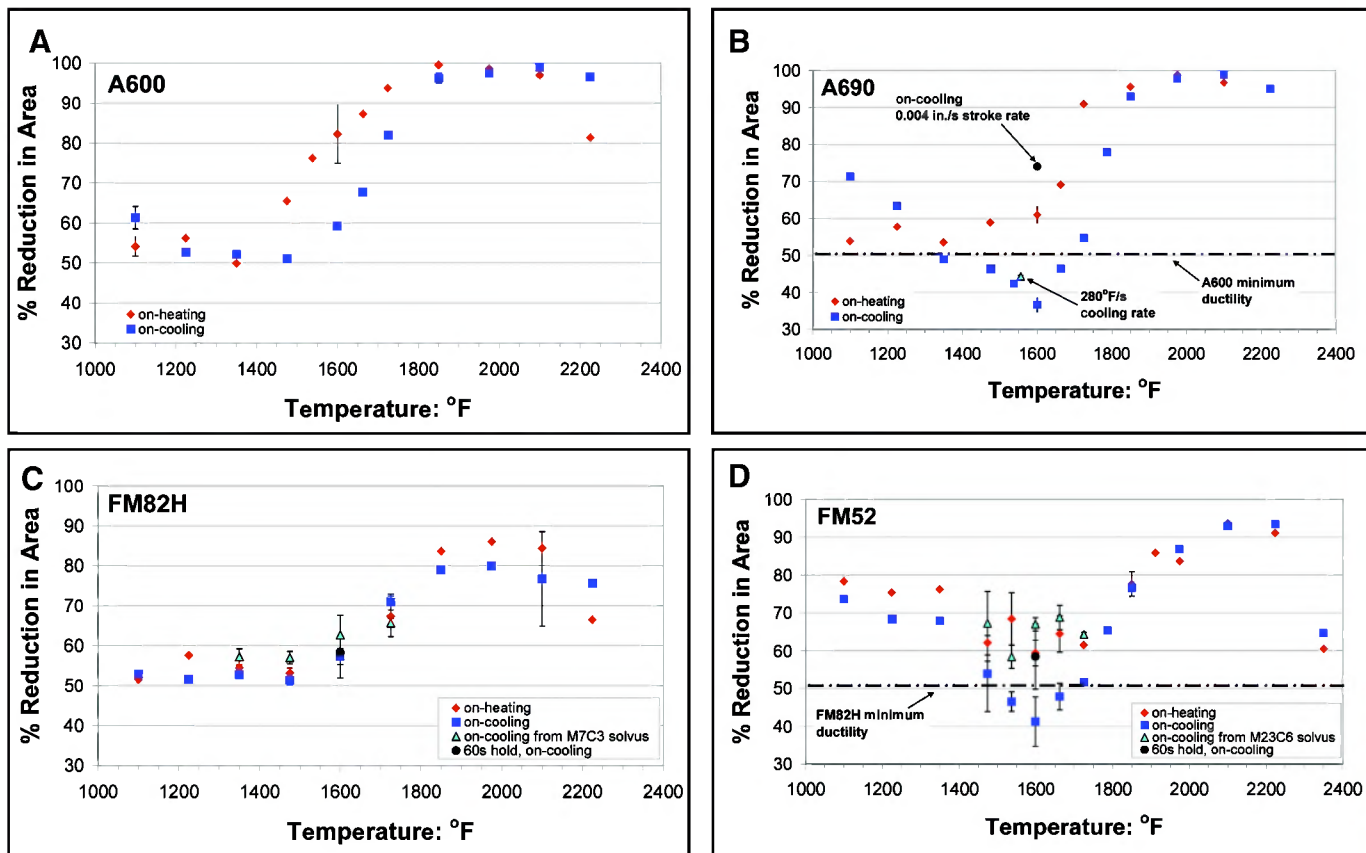


Fig. 1 — On-heating and on-cooling hot ductility curves for the following: A — A600; B — A690; C — FM82H; and D — FM52. FM82H and FM52 hot ductility curves also include on-cooling data from their respective carbide solvus temperatures.

shown to increase DDC susceptibility in 310 stainless steel (Ref. 4). However, recent testing performed on A690 has shown just the opposite effect, where decreasing the strain rate significantly improved the intermediate temperature ductility (Ref. 1). However, this difference may be the result of intergranular precipitation that was promoted by the increased time allotted by the slower strain rate. It has been shown that intergranular particles decrease grain boundary sliding (Refs. 5, 6), and both A690 and FM52 are strong intergranular $M_{23}C_6$ formers.

The second DDC hypothesis is impurity element embrittlement. Of all impurity elements, sulfur has the most detrimental effect in Ni and Ni-based alloys (Ref. 7). Nominal sulfur concentrations as low as 0.002 wt-% have been shown to have a dramatic effect on the ductility of

Ni over a wide range of temperature spanning from 20° to 1200°C (Ref. 8). Sulfur and phosphorous have also been implicated in the DDC of Invar (Refs. 9–11) and FM52 (Refs. 12, 13). The intergranular concentration of sulfur that will result in embrittlement of Ni has been found to be approximately 5 wt-% (9 at-%) (Refs. 14, 15). Other investigators have utilized auger electron spectroscopy to identify sulfur at grain boundaries in multipass welds of FM52 that were fractured in a high vacuum environment (Refs. 12, 16). However, since this analysis was performed on a multipass weld, it is impossible to know during which thermal cycle sulfur segregated to the grain boundaries (Ref. 12) or whether the segregation occurred after the ductility dip crack formed (Ref. 16). It has yet to be shown that sulfur is present at grain boundaries of FM52

at the point in the thermal cycle where ductility dip cracks form.

Intergranular precipitates are the third proposed mechanism for DDC. Intergranular MnS, MnO, AlN, and Al_2O_3 have all been found on DDC fracture surfaces in Invar (Ref. 17). Intergranular chromium-rich precipitates have also been observed on DDC fracture surfaces of 304 stainless steel (Ref. 18), FM82H (Ref. 19), and FM52 (Refs. 16, 19). It has been proposed that alloys that form $M_{23}C_6$ carbides, like FM52 and A690, are more prone to DDC (Refs. 16, 20). This is thought to be the result of localized interfacial stresses associated with the partially coherent $M_{23}C_6$ carbide. In contrast, alloys that form incoherent precipitates such as Ti(C,N), NbC, and M_7C_3 are generally not thought to exhibit DDC in multipass welds (Refs. 16, 20) because significant interfacial strains

Table 1 — Alloy Compositions (in wt-%)

	Ni	Cr	Fe	C	Mn	S	Si	Cu	Nb	Ti	Al	Ti + Al	P	Mo	Other
A600	75.67	14.87	8.22	0.079	0.36	0.001	0.25	0.01	—	—	—	—	—	—	—
FM82H	71.52	20.38	2.26	0.049	2.99	0.002	0.06	0.01	2.28	0.3	0.04	0.34	0.002	—	<0.5
A690	60.75	29.28	9.12	0.025	0.17	<0.001	0.08	0.01	<0.01	0.3	0.22	0.52	0.005	0.01	—
FM52	59.12	29.12	10.08	0.027	0.25	<0.001	0.13	0.01	<0.01	0.51	0.71	1.22	0.003	0.01	<0.5

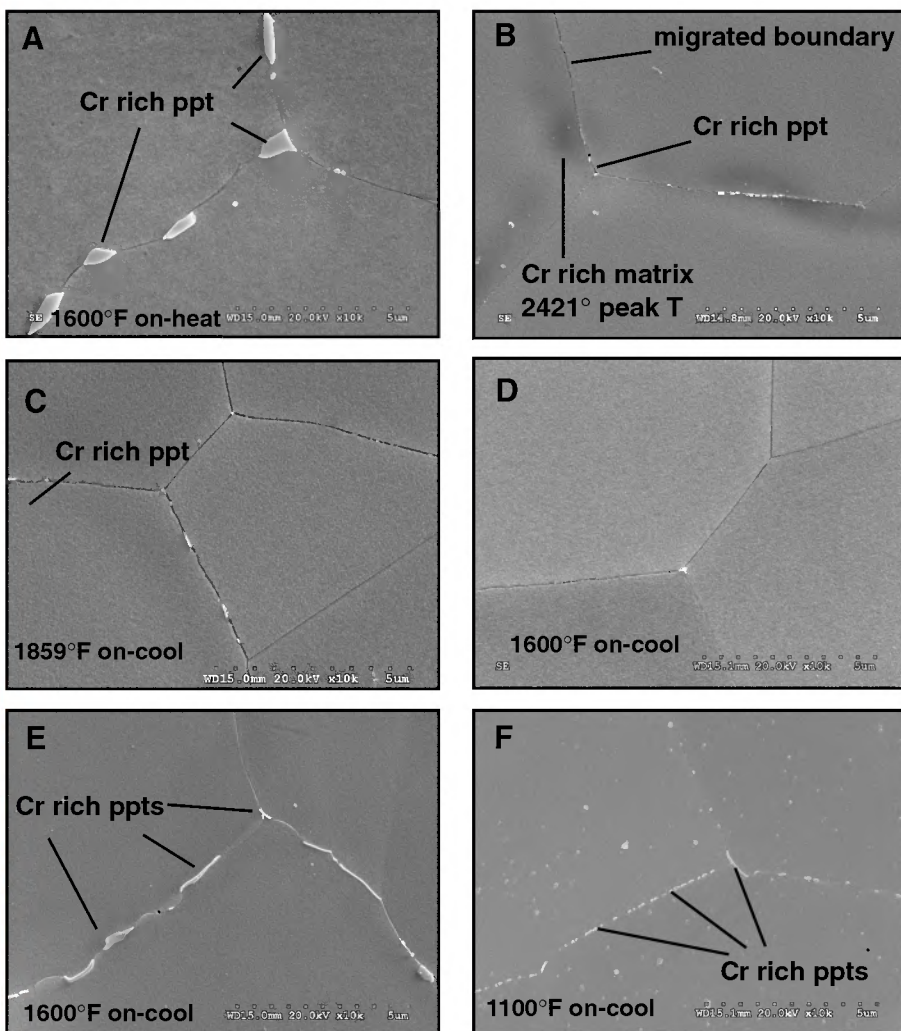


Fig. 2 — A600 water-quenched SEM micrographs. A — 1600°F on-heating; B — 2421°F peak temperature; C — 1859°F on-cooling; D and E — 1600°F on-cooling; and F — 1100°F on-cooling. EDS used to identify composition of various regions and precipitates indicated on micrographs.

are not expected. The exact role of intergranular precipitates on DDC remains unclear. Specifically, $M_{23}C_6$ may be the cause of DDC, contribute to it, or be merely coincidental.

Previous investigations into DDC have had several limitations in their experimental approach. Multipass weld mock-ups have been used to assess the DDC susceptibility of candidate filler metals (Refs. 20–22). However, these samples experience complex and multiple thermal-mechanical cycles that prevent accurate determination of microstructures, and/or microsegregants that cause ductility dip cracks to form. This problem can be resolved by using a hot tensile/Gleeble®-based test that exposes single-pass samples in the as-solidified condition to a simulated weld thermal cycle. Gleeble®-based testing has been used by several investigators, but only the heating or cooling portion of the weld thermal cycle has been investigated (Refs. 4, 19, 23–26). This is the sec-

ond limiting factor in previous work since reheated weld metal experiences both heating and cooling. To determine when the reheated weld metal is metallurgically most susceptible to form DDC, both the heating and cooling portions of the thermal cycle must be evaluated. There is a potential limitation of performing microstructural characterization on Gleeble specimens that are allowed to ‘free cool’ in the Gleeble vacuum jaws from their testing temperature. Preliminary testing showed that this method of cooling would result in cooling rates as low as 15°F/s in the sample design used for this work. This may allow enough time for diffusive processes to occur that can change segregation profiles and/or form secondary phases that may not have been present at the elevated temperature where the cracking susceptibility of the alloy was determined. Therefore, to minimize the potential for diffusional microstructural changes (e.g., precipitation, Sulfur segregation) that may occur during

‘free-cooling’ in the Gleeble, select samples were rapidly quenched from their test temperature for subsequent microstructural and microchemical characterization.

The objective of this work is to characterize the microstructural and microchemical development of A600, A690, FM82H, and FM52 during both heating and cooling portions of a simulated weld thermal cycle, and to correlate these microstructural changes to DDC susceptibility. As a first step, the majority of this characterization work was carried out on samples that were exposed to the weld thermal cycle, but without being strained. This approach captures the microstructure present immediately before strain was applied in the form of a Gleeble® hot ductility test as described in the first paper. The microstructural evolution in these unstrained samples will be compared to the DDC susceptibility of the alloys, which was determined in previous work (Ref. 1.) This work will provide further insight into the metallurgical mechanism(s) of DDC.

Experimental Procedure

Sample Preparation

A total of four alloys were investigated as part of this work: A600 (UNS: N06600), A690 (UNS: N06690), FM82H (AWS: ER-NiCr-3), and FM52 (AWS: ERNiCrFe-7). A600 and A690 were the two wrought alloys. FM82H and FM52 are the companion weld filler metals for A600 and A690, respectively. Nominal compositions for each alloy are given in Table 1. A600 and A690 form the base metal material in multipass weldments of many industrial applications and were therefore tested in the wrought condition as part of this work. The weld filler metals were tested in the as-solidified condition, which allowed the DDC susceptibility and microstructural evolution during the first weld thermal cycle to be studied. Details of the specimen design are presented elsewhere (Ref. 1).

Testing Parameters and Design

The heating rate for the on-heating tests was 200°F/s (111°C/s), while the cooling rate for all on-cooling tests was 90°F/s (50°C/s). He gas quench was used to augment the cooling rate in the “on-cooling” samples because the maximum “free cool” cooling rate that could be obtained in the Gleeble® was so low (15°F/s). The heating and cooling rates were based upon thermocouple measurements taken from a standard weld joint during typical multipass welding conditions. Samples were hot ductility tested at 125°F (51°C) intervals between 1100°F (593°C) and the peak temperature for each alloy. Smaller tem-

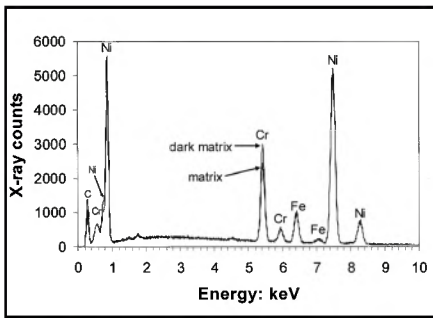


Fig. 3 — Two EDS spectra from A600 2421°F peak temperature superimposed on one another. The “dark matrix” refers to the “Cr-rich matrix” region in Fig. 2B. Sample was water quenched.

perature intervals of 62.5°F (17°C) were used in some cases to provide more detail within temperature ranges of interest. The details of the testing parameters are presented elsewhere (Ref. 1).

To better understand how microstructure and microchemistry affected DDC susceptibility, several samples from each alloy were water quenched at select temperatures along the weld thermal cycle. These temperatures were based upon the results of hot ductility testing. In an actual multipass weld, the weld metal experiences a complex combination of thermal and mechanical influences. As a first step, only the thermal influences on microstructural evolution were investigated with the majority of samples in this work. These samples were not strained when they were water quenched at the temperatures of interest. The cooling rates obtained using the water quench were in excess of 3000°F/s. The combined effect of thermal and mechanical influences was examined with a limited number of samples that were water

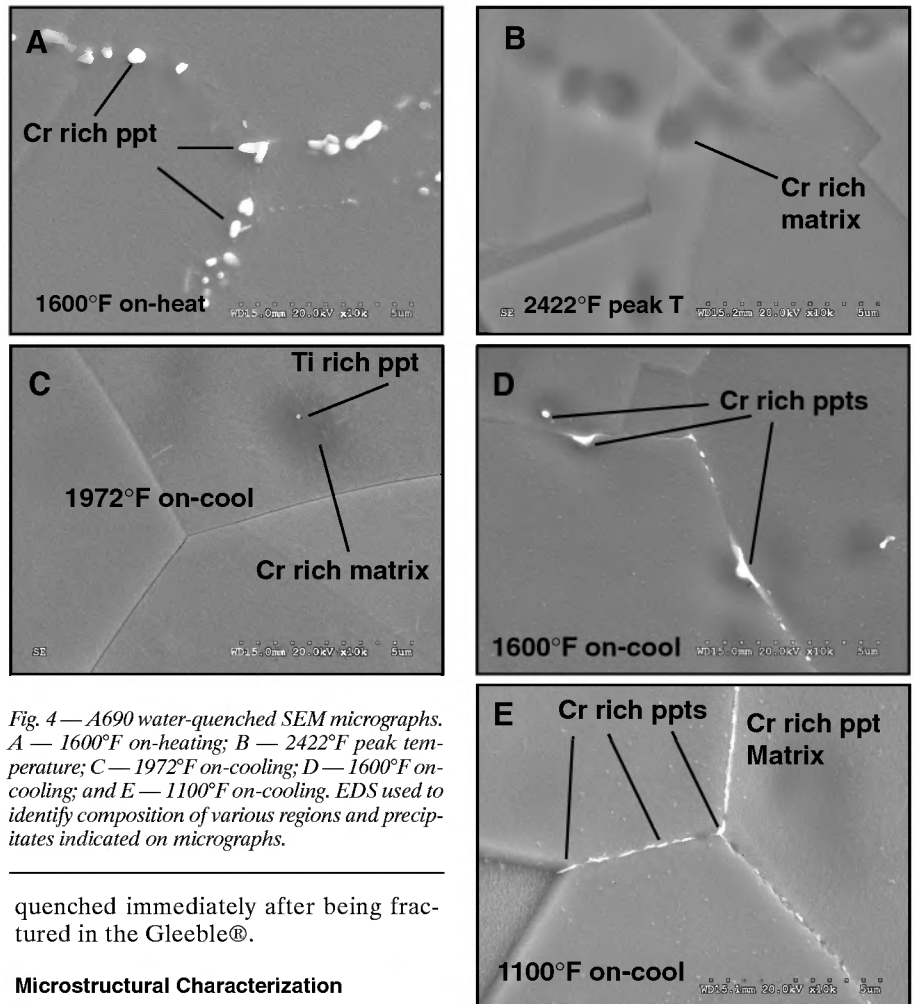


Fig. 4 — A690 water-quenched SEM micrographs. A — 1600°F on-heating; B — 2422°F peak temperature; C — 1972°F on-cooling; D — 1600°F on-cooling; and E — 1100°F on-cooling. EDS used to identify composition of various regions and precipitates indicated on micrographs.

quenched immediately after being fractured in the Gleeble®.

Microstructural Characterization

Samples were sectioned and mounted in thermosetting epoxy so that the following surface could be viewed: longitudinal-transverse orientation for the base metal and parallel to the welding direction-transverse for the weld metal samples.

Standard metallographic techniques were used to prepare the samples to a 0.05- μ m colloidal silica finish. After final polishing, the samples were ultrasonically cleaned in ethanol, followed by distilled water. This step was found to be effective at removing

Table 2 — Grain diameter data as a function of temperature along first reheat thermal cycle.

Temp (°F)	A600 Grain diam. (μ m)	Std. dev. (μ m)	Temp (°F)	A690 Grain diam. (μ m)	Std. dev. (μ m)
BM	41	7	BM	29	7
1100 on-heat	41	5	1100 on-heat	30	2
1600 on-heat	42	7	1600 on-heat	25	3
1859 on-heat	41	4	1972 on-heat	35	20
2422 peak T	50	8	2422 peak T	52	10
1859 on-cool	57	8	1972 on-cool	86	11
1600 on-cool	98	27	1600 on-cool	93	13
1100 on-cool	196	54	1100 on-cool	101	11

Table 2 — (continued)

Temp (°F)	EN82H Grain diam. (μ m)	Std. dev. (μ m)	Temp(°F)	EN52 Grain diam. (μ m)	Std. dev. (μ m)
As-solidified	153	36	As-Solidified	294	40
1600 on-cool from 1967	158	38	1600 on-cool from 2077	269	51
1600 on-cool	142	34	1600 on-cool	263	50
1600 on-cool	158	38	1600 on-cool 2077	269	51
60-s hold @ 1600	144	38	60-s hold @ 1600	293	50

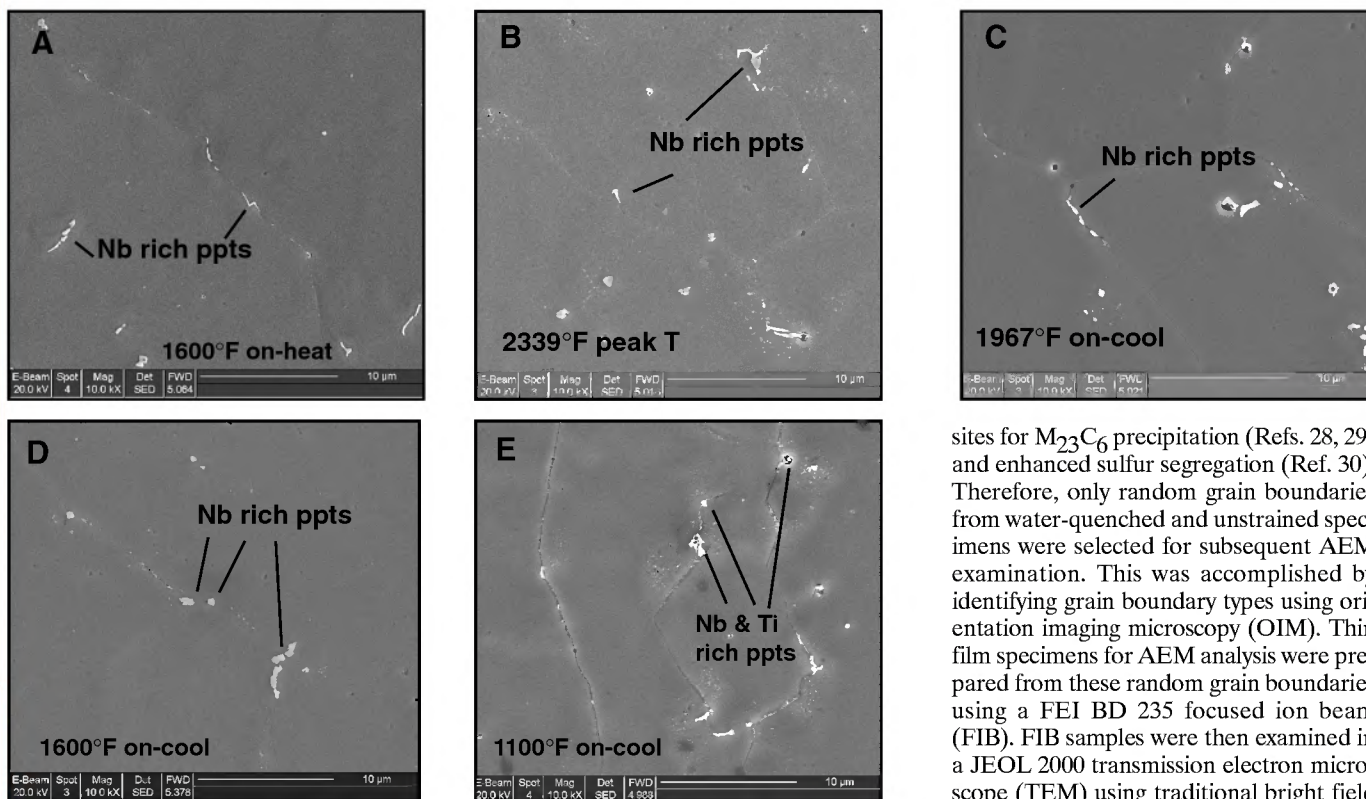


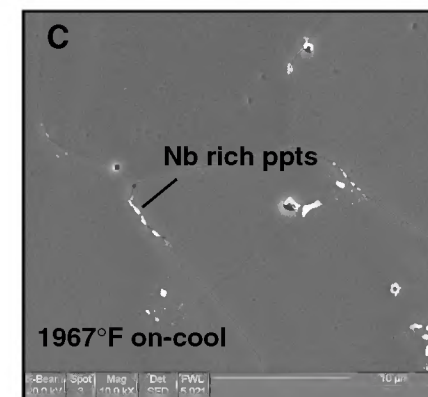
Fig. 5 — FM82H water-quenched SEM micrographs. A — 1600°F on-heating; B — 2339°F peak temperature; C — 1967°F on-cooling; D — 1600°F on-cooling; and E — 1100°F on-cooling. EDS used to identify composition of various regions and precipitates indicated on micrographs.

polishing media from intergranular crack surfaces while preserving their microstructure. The samples were then electrolytically etched at 2–3 V for 3–10 s in a solution containing equal parts by volume of water and sulfuric and phosphoric acid. Grain size measurements were carried out on water-quenched specimens using the Abrams Three-Circle procedure as detailed in ASTM E112 (Ref. 27). This method compensates for nonequiaxed grain shapes, which is to be expected in the weld metal samples.

The general microstructure and chemistry of second phases was characterized using either an FEI DB 235 or Hitachi 4300 Schottky field emission gun scanning electron microscope (FEG-SEM) with an energy-dispersive spectrometer (EDS).

All operation was performed using 20-keV accelerating voltage. An Everhart-Thornley detector, commonly known as a secondary electron detector (SED), was used for all SEM images. The scale markers differ for the two microscopes. Images captured using the Hitachi 4300 use a 10-dot marker with the scale indicated on the lower right corner of the image. Samples mounted in epoxy were lightly coated with carbon to prevent charging. These FEG-SEMs and operating conditions enabled particles as small as 20 nm in size to be resolved.

Previous research has shown that grain boundaries with random orientations are the most susceptible to ductility dip cracks (Ref. 24). It has also been shown that these same random boundaries are preferential

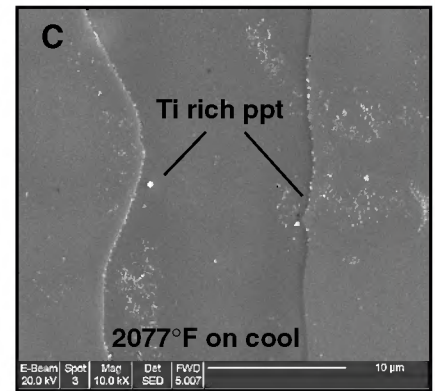
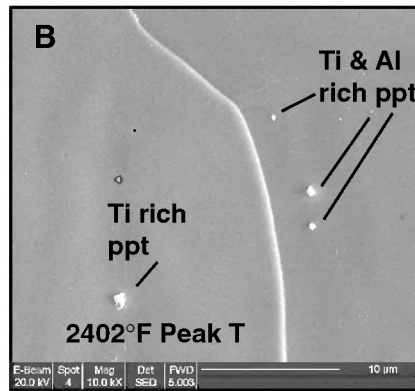
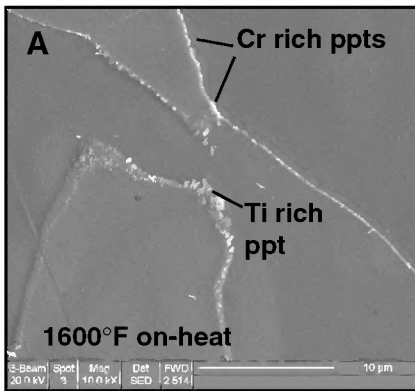


sites for $M_{23}C_6$ precipitation (Refs. 28, 29) and enhanced sulfur segregation (Ref. 30). Therefore, only random grain boundaries from water-quenched and unstrained specimens were selected for subsequent AEM examination. This was accomplished by identifying grain boundary types using orientation imaging microscopy (OIM). Thin film specimens for AEM analysis were prepared from these random grain boundaries using a FEI BD 235 focused ion beam (FIB). FIB samples were then examined in a JEOL 2000 transmission electron microscope (TEM) using traditional bright field and dark field imaging techniques. The grain boundary chemistry of the thin films were examined in a VG 603 dedicated scanning transmission analytical electron microscopy (AEM), operated at 300 kV and fitted with a Nion spherical aberration corrector.

The VG 603 was used to generate compositional maps, line scans, and point analyses using EDS, and capture dark field images using a high-angle annular dark field detector (HAADF). The compositional maps were 128×128 pixels in size and collected using a 200-ms dwell time at each pixel. An EDS spectrum file was generated for each map. Background subtracted compositional maps were generated for each element of interest using the computer software program Digital Micrograph version 1.6.1 by integrating the number of counts in the K_{α} peak of each element of interest and subtracting that by a background window. The point analyses and line scans were collected using 120 s of live time per point, which did not result in any specimen contamination or discernable damage. The composition of Fe, Ni, and Cr were quantified using the Cliff-Lorimer technique (Ref. 31), and integrated K_{α} peak intensities that were background subtracted for each element. The measurement error of each AEM data point was calculated using the quadrature sum technique (Ref. 32). Experimentally determined Cliff-Lorimer sensitivity factors or “k-factors” were generated from an FM52 sample that was homogenized by isothermal hold for 10 min at 2350°F (1288°C) in the Gleeble®, then water quenched.

Table 3 — JMatPro Calculated Carbide Solvus Temperatures for the Predominant Carbides in Each Alloy and the Time above Calculated Carbide Solvus Temperatures during Simulated Weld Reheat Thermal Cycle

Alloy	Intergranular Carbide	Calculated Carbide Solvus (°F)	Time above Calculated Carbide Solvus (s)
A600	M_7C_3	1859	9.1
FM82H	MC	2196	2.3
FM82H	M_7C_3	1967	6.0
A690	$M_{23}C_6$	1972	7.3
FM52	$M_{23}C_6$	2077	5.3



Results

Grain Size Measurements

The grain size measurements for all four alloys are presented in Table 2. The carbide solvus temperatures for each alloy were calculated using JMatPro 3.0 (Ref. 1) and are presented in Table 3. The grain size for A600 and A690 are constant until the carbide solvus temperature is exceeded. The scatter in the A600 grain size data increases as the alloy continues to cool past the M_7C_3 solvus temperature (1859°F (1015°C)). There is less scatter in the grain size data of A690. The average grain size of FM82H and FM52 remains stable, even though the standard deviation is larger than that observed for the two wrought alloys.

Microstructural Characterization: SEM

The thermal effects on the microstructural evolution of the four alloys during the first thermal cycle are shown in Figs. 2 through 6. The microstructures at five key temperatures are displayed for each alloy. The first micrograph is for 1600°F (871°C) on-heating. In all four alloys there was no microstructural change observed between the starting condition (wrought or as-solidified) up to the carbide solvus temperature on-heating. Therefore, the 1600°F (871°C) on-heating micrograph is representative over this range of temperatures. The grain boundaries of all alloys were decorated with carbides in their starting condition and up to their respective carbide solvus temperatures. In A600 the grain boundaries are decorated with globular chromium-rich precipitates, which have previously been shown to be M_7C_3 carbides (Refs. 33, 34). In A690 chromium-rich $M_{23}C_6$ carbides are predominant (Refs. 28, 35). Both intra and intergranular Nb-rich MC carbides are present in FM82H (Ref. 36). FM52 contains both titanium- and chromium-rich second phases. The titanium-rich phase is a carbo-nitride and occurs both intra and intergranularly, while the chromium-rich phase is $M_{23}C_6$, and is only found inter-

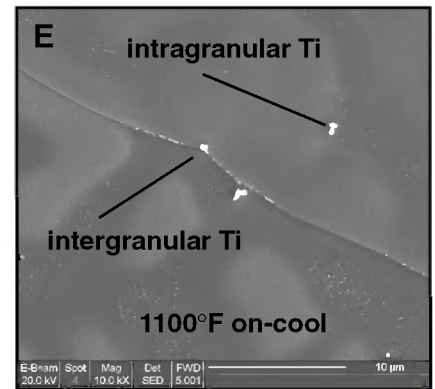
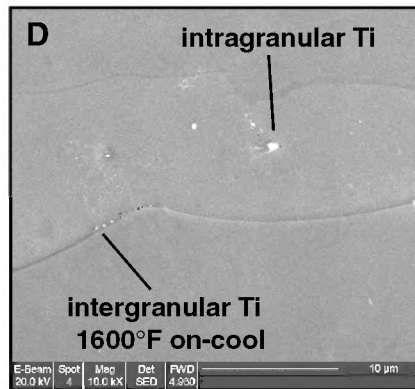


Fig. 6 — FM52 water-quenched SEM micrographs. A — 1600°F on-heating; B — 2402°F peak temperature; C — 2077°F on-cooling; D — 1600°F on-cooling; and E — 1100°F on-cooling. EDS used to identify composition of various regions and precipitates indicated on micrographs.

granularly (Ref. 36). Because the phases formed in each alloy are well known, only EDS was used to qualitatively confirm the types of the second-phase particles.

The second micrograph is for the peak temperature of each alloy, which corresponds to the nil strength temperature (NST) -25°F. At this temperature the microstructural development differs for each alloy. In A600 there was partial dissolution of intergranular carbides. Additionally, a small degree of grain boundary migration was observed in grain boundaries that were no longer pinned by carbides. The carbide dissolution produced dark regions in the matrix as seen in Fig. 2B. The composition of these dark regions was ana-

lyzed using EDS and compared to the matrix, as seen in Fig. 3. The integrated x-ray counts in the chromium peak of the dark region were found to be 9% greater than in the matrix, confirming that the dark region was enriched in chromium. These EDS results are corroborated by the atomic number contrast exhibited between the chromium-rich region and the matrix. Increasing chromium concentration will decrease the average atomic number, which causes these regions to appear darker.

At the peak temperature in A690 and FM52 (Figs. 4B and 6B), there was complete dissolution of chromium-rich carbides. Chromium-rich regions in the A690

Table 4 — AEM Point Data for FM52 Specimens from Various Thermal Conditions. Absolute Error for Each Element in wt-% is as Follows: Ni ± 0.9, Cr ± 1.2, Fe ± 1.2

Condition	Location	Ni	Cr	Fe
1600°F on-heating	Grain boundary	66.3	21.4	10.5
	Matrix	58.9	29.8	9.6
	Precipitate	13	81.5	3.8
1600°F on-cooling	Grain boundary	57.9	30.4	9.9
	Matrix	58.3	30.2	9.7
	Precipitate	no Cr-rich precipitates		
60-s hold at 1600°F on-cooling	Grain boundary	65.9	21.2	11.2
	Matrix	58.7	29.6	9.9
	Precipitate	11.4	83.1	3.5

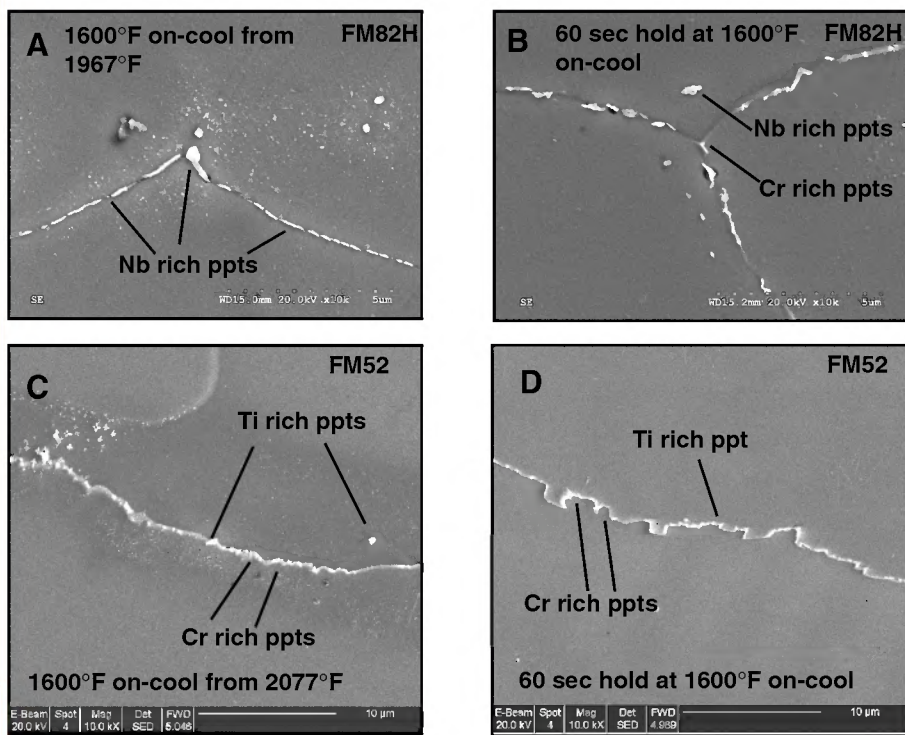


Fig. 7 — SEM micrographs of FM82H (A and B) and FM52 (C and D) that were water quenched at 1600°F on-cooling from the carbide solvus temperature (A and C), and water quenched after a 60-s hold at 1600°F on-cooling from NST-25°F.

matrix remained where intergranular carbides were once located, similar to A600. These chromium-rich regions traced out the former location of grain boundaries, which had all migrated away from their original locations. The only second phases existent at the peak temperature of both A690 and FM52 were Ti(C,N). There is no discernable microstructural change in A690 and FM52 at the on-cooling $M_{23}C_6$ solvus temperature (Figs. 4C and 6C), which is 1972°F (1078°C) and 2077°F (1136°C), respectively. Extensive interrogation of precipitates using EDS revealed that only Ti(C,N) precipitates remain over this temperature range. For example, all the second phases present in Fig. 6C contain titanium, thereby precluding them from being $M_{23}C_6$. However, at 1600°F (871°C) on-cooling there are intergranular chromium-rich carbides in A690 that are not present in FM52 at the same temperature. These chromium-rich intergranular precipitates are found to be inhomogeneously precipitated on A690 grain boundaries that intersect the chromium-rich regions of the matrix that remain after the dissolution of blocky $M_{23}C_6$ intergranular carbides. Figure 4D shows a region where the grain boundary carbide coverage is relatively high for this alloy and temperature; however, much of the grain boundary length was free of chromium-rich carbides. In both A600 and A690 the intergranular carbide cover-

age is much greater on-heating than it is on-cooling.

The carbide dissolution behavior in A600 is distinctly different than in A690 and FM52. In A600 there are regions of grain boundaries where the intergranular carbides never fully dissolve during the super solvus portion of the thermal cycle. This is shown in Fig. 2C, which is taken on-cooling at the M_7C_3 solvus for A600 (1859°F (1015°C)). As the alloy cools these carbides coarsen, as shown in Fig. 2D, which is taken at 1600°F (871°C) on-cooling. The carbide content may also increase due to precipitation below the carbide solvus temperature. However, this intergranular carbide coverage is not uniform, as some boundaries contain very few precipitates, as seen in Fig. 2E, which is at 1600°F (871°C) on-cooling. In this region the carbides fully dissolved and have yet to reprecipitate. Additionally, both the intergranular carbide morphology and grain boundary carbide coverage for both A600 and A690 at 1600°F (871°C) on-cooling is significantly different than at 1600°F on-heating. The micrographs shown in Figs. 2D and 4D represent the greatest amount of intergranular precipitation observed in both A600 and A690 at 1600°F on-cooling.

There were three different levels of intergranular carbide dissolution observed with the four alloys. A690 and FM52 experienced complete intergranular chromium-carbide dissolution, while the

chromium-carbide dissolution in A600 was incomplete. In FM82H there was no discernable dissolution of the NbC precipitates throughout the thermal cycle. Qualitatively, it appeared that there may be a slight increase in intergranular NbC precipitates at the peak temperature as seen in Fig. 5B. The FM82H microstructure remains very stable, as can be seen in the micrographs at 1600°F (871°C) and 1100°F (593°C) on-cooling.

The microstructural results from modifying the thermal cycle in FM82H and FM52 are shown in Fig. 7. Increased intergranular carbide coverage was observed when the peak temperature was lowered to the respective carbide solvus for each alloy. The time at the solvus temperature was short (less than 0.25 s) and insufficient to cause any carbide dissolution. An isothermal hold at the on-cooling ductility minimum temperature (1600°F (871°C)) for 60 s also produces increased intergranular carbides in both alloys. Additionally, some of the grain boundaries in FM52 become more serrated as a result of the isothermal hold.

Microstructural and Microchemical Characterization: AEM

The experimentally determined Cliff-Lorimer sensitivity factors and associated standard deviation were found to be $k_{FeNi} = 0.913 \pm 0.0068$ and $k_{CrNi} = 0.861 \pm 0.0044$. The thin foils prepared using the FIB technique were first examined using a TEM to determine that they were suitable for subsequent analysis. This examination involved using electron diffraction to confirm the location of grain boundaries prior to analysis in the AEM. All of the boundaries are oriented vertically in the following AEM maps. Figure 8 displays the AEM results from an FM52 1600°F on-heating. The dotted line in the HAADF image denotes the grain boundary. Chromium-rich precipitates are observed adjacent to a titanium-rich precipitate. No sulfur or phosphorus were detected in the AEM maps collected from this condition, nor were they detected in any spot analysis performed on the boundary or in the matrix. Table 4 contains quantified point analyses data collected from the grain boundaries and matrix. It was found that the grain boundaries in FM52 at 1600°F on-heating were depleted in Cr (21.4 vs. 29.8 wt-%) and enriched in Ni (66.3 vs. 58.9 wt-%) as compared to the matrix, while there was no difference in Fe concentration (~10 wt-%) given the experimental error.

The AEM mapping results for FM52 1600°F (871°C) on-cooling from the NST-25°F temperature are presented in Fig. 9. The dotted line in the HAADF image denotes the grain boundary. No chromium-

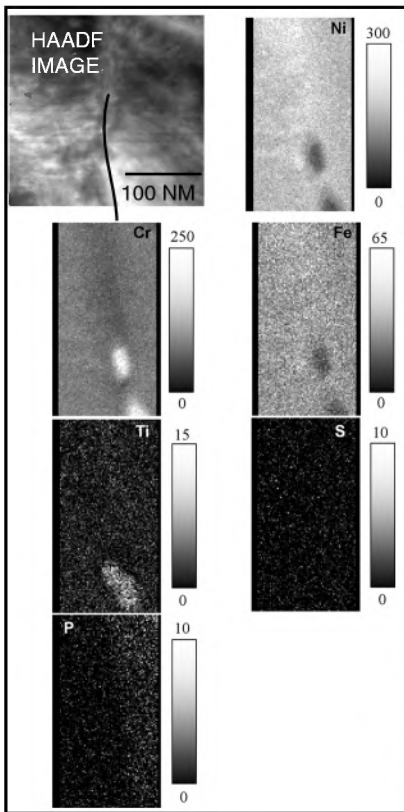


Fig. 8 — AEM results from FM52 1600°F on-heating, water-quenched sample. Dotted line in HAADF image delineates grain boundary. Grayscale bar indicates number of integrated x-ray peak counts above background.

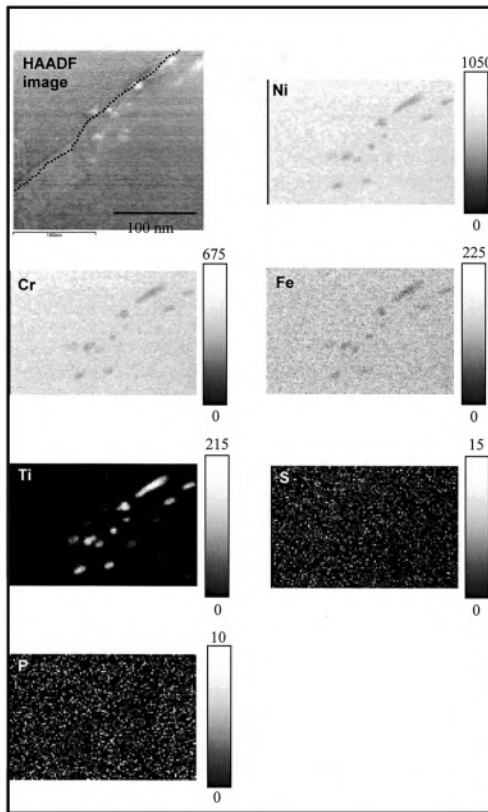


Fig. 9 — AEM results from FM52 1600°F on-cooling from NST-25°F, water-quenched sample. Dotted line in HAADF image delineates grain boundary. Grayscale bar indicates number of integrated x-ray peak counts above background.

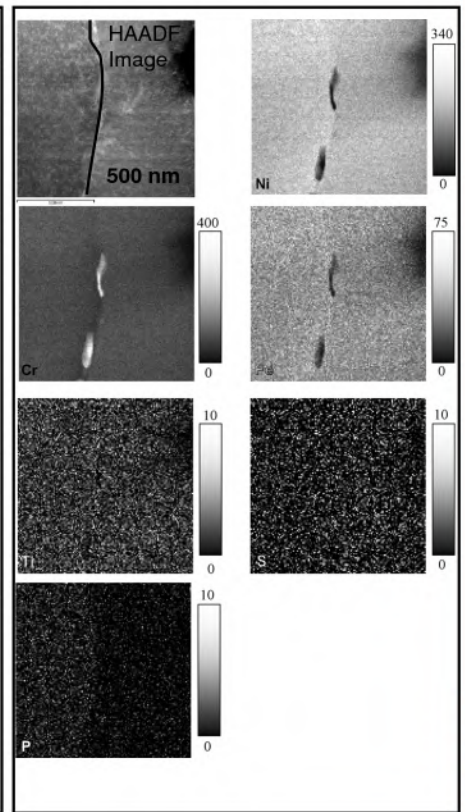


Fig. 10 — AEM results from FM52 60-s hold at 1600°F on-cooling from NST-25°F, water-quenched sample. Dotted line in HAADF image delineates grain boundary. Grayscale bar indicates number of integrated x-ray peak counts above background.

rich precipitates were observed in this condition; however, titanium precipitates are observed along the grain boundary. The smallest precipitate that was resolved in all of the AEM work was a seven-nm-diameter titanium precipitate in this thermal condition. The concentrations of iron, nickel, and chromium along the grain boundary in the composition maps are indistinguishable from those in the matrix. This similarity is quantified by use of spot measurements, which are recorded in Table 4. This shows that not only did the peak temperature portion of the thermal cycle dissolve the chromium-rich carbides, but it homogenized the near grain boundary concentration profiles of nickel and chromium that were existent at 1600°F (871°C) on-heating.

Figure 10 shows the results for FM52 after a 60-s hold at 1600°F (871°C) on-cooling from the NST-25°F temperature. Larger chromium-rich intergranular precipitates are observed in this condition, which necessitated that the compositional map displayed in Fig. 10 be collected at a lower magnification than for the 1600°F on-heating and 1600°F on-cooling conditions. Like these other two conditions, no sulfur or phosphorous was detected in any

AEM map, nor in any point analysis in the 60-s hold condition. Like the 1600°F on-heating condition, there is chromium depletion (21.2 vs. 29.6 wt-%) and nickel enrichment (65.9 vs. 58.7 wt-%) along the grain boundaries as compared to the matrix. The chromium concentration adjacent to the precipitate-matrix interface is different on each side of the precipitate, as seen in Fig. 11. The interface that the precipitate has with the grain on the right exhibits no chromium depletion (~29.5 wt-% Cr), while the chromium concentration at the interface the same precipitate has with the other grain is only approximately 24 wt-% on one side of the precipitate.

The detectability of any element using EDS is a function of collection live time (Ref. 37). Therefore, to improve the detectability of sulfur and phosphorous, EDS spectra collected from multiple AEM maps and point analyses were summed. This was performed for data collected from FM52 specimens quenched at the ductility minimum temperature, 1600°F (871°C) on-cooling from NST-25°F. EDS data from nearly 23,000 pixels located near grain boundary region of 13 different boundaries were added, which resulted in the EDS spectrum in Fig. 12A.

This summed EDS spectrum had a total live time of 76 min. No sulfur or phosphorous were detected. Similarly, EDS spectra from multiple 120-s live time point analyses were summed to produce Fig. 12B, which had a total live time of 16 min. Once again, there was no evidence of sulfur or phosphorous.

Fractography

A ductility dip crack from an FM52 specimen tested at 1600°F on-cooling that was water quenched immediately after fracture is shown in Fig. 13. The fracture surface contains both dimpled and wavy regions. The wavy regions are the dominant fracture surface appearance in ductility dip crack of all four alloys. The fracture surface is decorated with chromium-rich precipitates, as determined by EDS, that are 200–300 nm in width (Fig. 13B). Intergranular precipitates with similar size, morphology, and chemistry (chromium rich) are observed on the grain boundary adjacent to ductility dip crack (Fig. 13C and D). Intergranular cavities are found adjacent to these precipitates, as seen in Fig. 13D.

For the purpose of comparison, Fig. 14

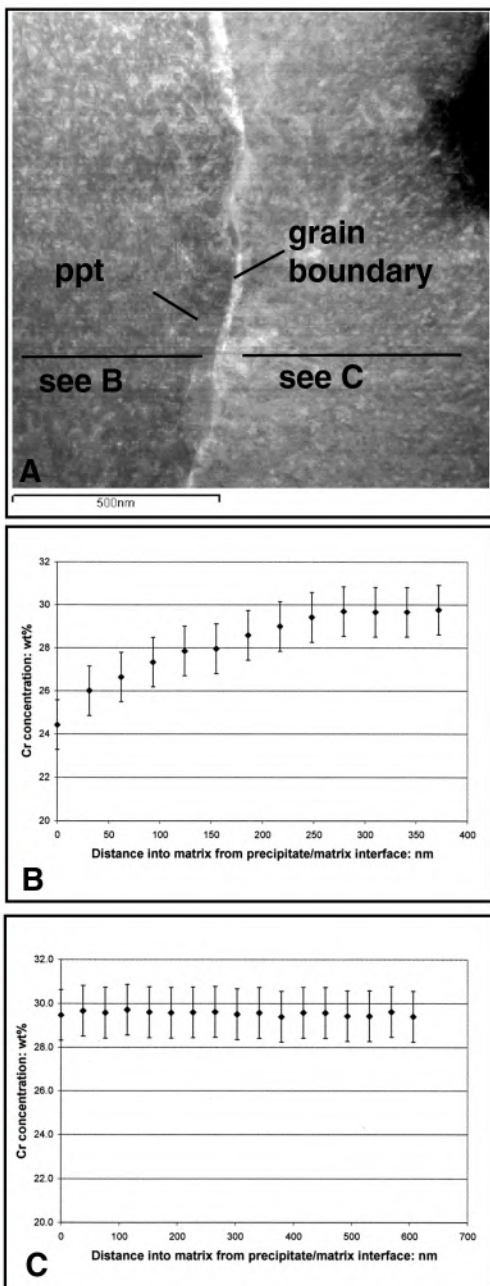


Fig. 11 — AEM chromium concentration profiles as a function of distance from precipitate matrix interface in the FM52 60-s hold at 1600°F on-cooling water quenched sample. HAADF image in A is the same as that in Fig. 10; B and C are the chromium concentration profiles to the left and right of the precipitate, respectively.

is a SEM fractograph of a ductility dip crack taken from a multipass weld of FM52 that was fabricated as part of previous work (Refs. 22, 20). The fracture surface of the multipass weld is quite similar to the DDC fracture surface in the Gleeble® hot ductility specimen (Fig. 13). Each fracture surface exhibits a wavy appearance and is decorated with chromium-rich carbides that are approximately 200–300 nm in size.

Figure 15 is the fracture surface from an FM52 specimen held at 1600°F (871°C) for 60 s before being hot ductility tested. The

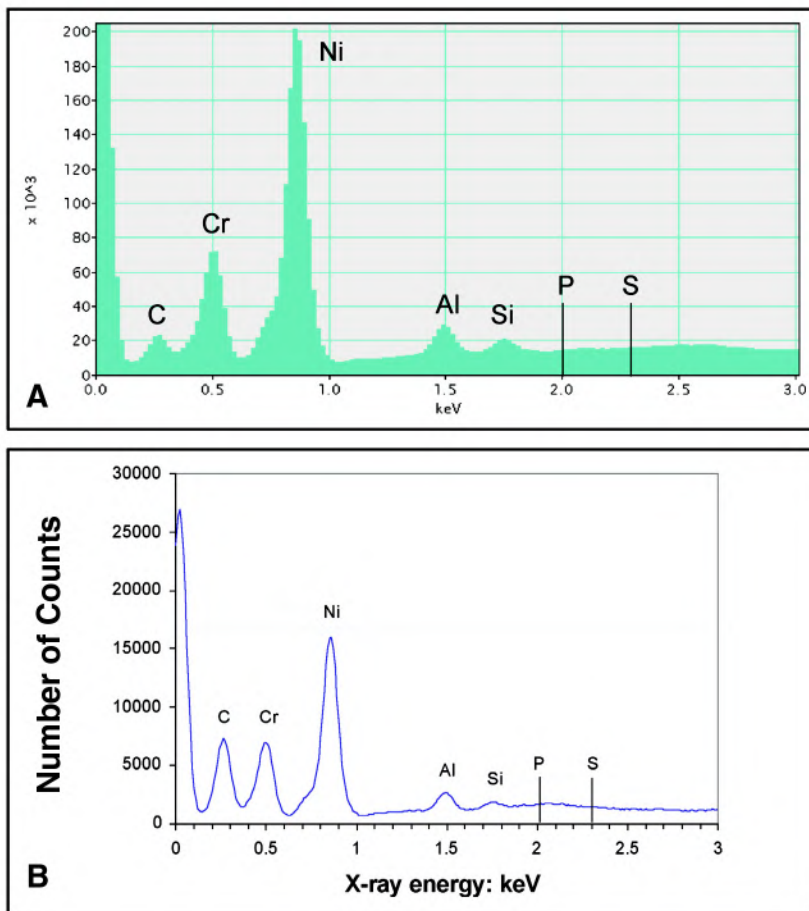


Fig. 12 — EDS spectra from FM52 water quenched at 1600°F on-cooling from NST-25°F grain boundary regions. A — Sum from compositional maps; B — sum from point analyses.

tensile axis is oriented in the horizontal direction. This crack shares some similar features with those observed in the specimen fractured at 1600°F without any hold (Fig. 13). Additionally, in both conditions the samples have intergranular cavities along the grain boundary adjacent to the ductility dip crack. The difference is that the precipitates in the 60-s hold specimen are significantly larger and have a disc shape (Fig. 15B and C) compared to those observed in the sample without the hold. The interprecipitate cavities are also clearly seen between the precipitate discs on the fracture surface in Fig. 15D.

Discussion

Influence of Microstructure on Grain Size Evolution

The changes in grain size throughout the thermal cycle are a function of the precipitate dissolution behavior. In A600 and A690 the grain size remains stable on-heating up the respective carbide solvus temperature. This is the result of intergranular carbides pinning the boundaries

and preventing them from migrating. Other investigators have reported similar findings for A690 (Refs. 38–40). At temperatures above the carbide solvus the grain size of A690 begins to increase considerably while that of A600 only changes slightly. This is the result of the complete dissolution of intergranular carbides in A690 and incomplete dissolution in A600. As the temperature continues to decrease on-cooling the grain size in A690 stabilizes due to the formation of intergranular precipitates at locations where the boundary intersects chromium-rich regions in the matrix that are remnants of previously dissolved intergranular carbides. In A600 the grain boundaries that contain carbides remain pinned, while those that do not contain carbides continue to migrate even as the temperature drops to 1100°F (593°C) on-cooling. It is for these reasons that the grain size standard deviation for A600 at 1600°F (871°C) and 1100°F on-cooling is so large.

While the grain size varies with temperature in the wrought alloys it is essentially constant in both of the weld metal alloys, FM82H and FM52. The stable average grain size for the two weld metals can be at-

tributed to two factors. First, the driving force for grain growth is inversely proportional to grain size. The as-solidified grain size in FM52 is nearly 10 times greater than that in A690; therefore, there is much less driving force for grain growth in FM52 than in A690. The second cause for the stable average grain size is shown in Figs. 5 and 6. There are intergranular Nb- and Ti-rich precipitates in FM82H and FM52, respectively, which never fully dissolve during the peak temperature portion of the thermal cycle. The NbC second phases are not expected to dissolve before liquation would occur because they are a terminal solidification product. These precipitates pin the grain boundaries and prevent grain growth in just the same way as was seen for A600 and A690 on-heating. There is a larger standard deviation about the average grain size in both the weld alloys as compared to the wrought alloys. This variation is not the result of abnormal grain growth since there was no evidence of large scale grain boundary migration. This variation can be attributed to the competitive grain growth that occurs during solidification of the weld metal. Grains that have their easy growth direction ($\langle 100 \rangle$ in face-centered cubic) oriented in the direction of

the maximum heat extraction (temperature gradient) will grow the fastest, resulting in the largest grains in the solidified weld metal. These fast growing grains will crowd out the growth of grains where the easy growth direction is not as favorably oriented to the direction of heat flow.

Although the grain size for FM52 ranges from 3 to 10 times larger than that of A690, they both exhibit a very similar ductility minimum ($\sim 38\%$ RA) and increase in ductility dip cracking at 1600°F (871°C) on-cooling. The grain sizes of A600 and A690 at 1600°F are similar, yet at this same temperature A690 has a significantly lower ductility and higher normalized ductility dip crack length (Ref. 1). Thus, the observed differences in DDC susceptibility cannot be explained by grain size.

Microstructural and Microchemical Characterization: AEM

The FEG-SEM combines good resolving power with the ability to examine a comparatively large surface area (compared to the TEM), which was approximately $10^6 \mu\text{m}^2$ in the case of the samples examined in this work. However, its analytical resolution is limited to approximately $1 \mu\text{m}^3$ due to incident electron-specimen interactions that occur in bulk specimens. Conversely, the analytical resolution of FEG analytical electron microscope (FEG-AEM) permits detection

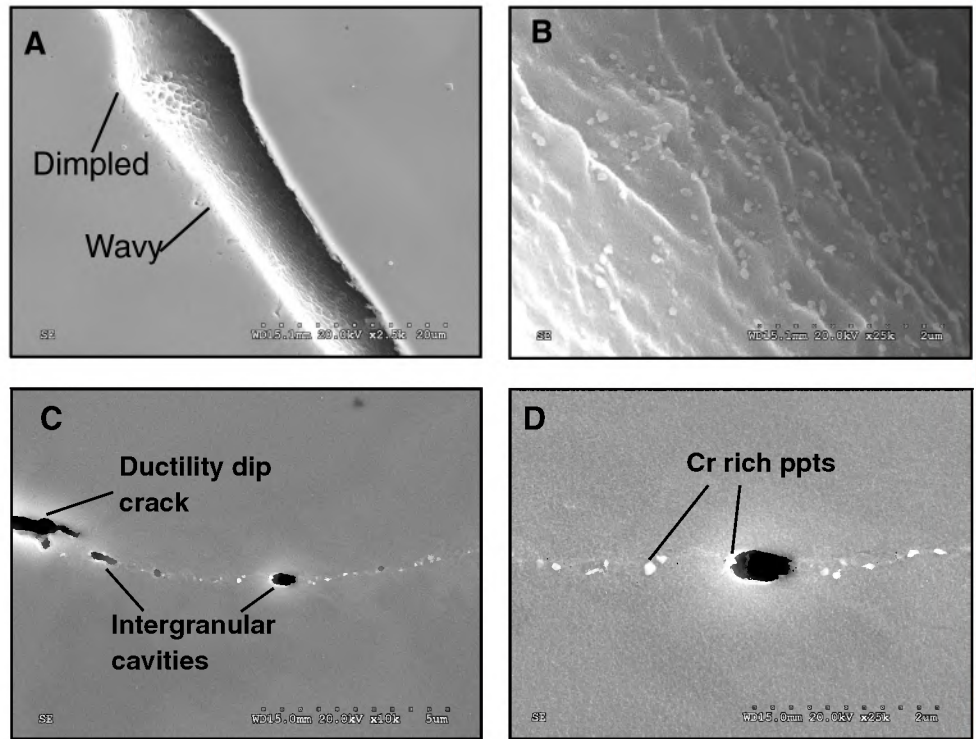


Fig. 13 — SEM micrographs of ductility dip crack in FM52 1600°F on-cooling hot ductility sample, immediately water quenched after fracture. A — Ductility dip crack with both dimpled and wavy regions; B — precipitates on the fracture surface in wavy region of A; C and D — precipitates along grain boundary adjacent to ductility dip crack in A and B.

down to $10^{-5} \mu\text{m}^3$ (Ref. 37), but the total sample surface area that can be examined is limited to approximately $100 \mu\text{m}^2$.

For the above reasons, specimens to be examined using AEM must be carefully selected so that they are representative. It has been shown that DDC is most likely to form on grain boundaries that have a random coincident site lattice (CSL) orientation (Ref. 24). Random boundaries have also been shown to be more prone to form M_{23}C_6 precipitates in A690 (Ref. 28) and 304 stainless steel (Ref. 29) due to the greater surface energy associated with random boundaries. In grain boundary segregation studies performed using high purity nickel doped with sulfur, random boundaries were found to have the greatest degree of sulfur segregation (Ref. 30). Therefore, of all grain boundaries that could be examined in the AEM, random grain boundaries are the most important since they are most susceptible to ductility dip cracking, forming precipitates, and having impurity elements segregate to them. In this work only random boundaries were examined in the TEM and AEM.

The AEM maps were performed at magnifications ranging from 100,000 to 1,000,000 \times . Each pixel ranged from 9.1 to 0.91 nm in size. The AEM results corroborate the SEM observations that intergranular chromium-rich precipitates were present in FM52 when the DDC resist-

ance at 1600°F (871°C) was high: at both 1600°F on-heating and after a 60-s hold at 1600°F on-cooling. At the ductility minimum temperature in FM52 (1600°F on-cooling) there were no chromium-rich carbides observed in the FEG-SEM or AEM. Only precipitates containing titanium were observed in the water quenched, unstrained samples examined in the FEG-SEM or AEM. The smallest second phase resolved in the AEM work was 7-nm-diameter titanium-rich precipitate; therefore, if chromium-rich precipitates are present at 1600°F on-cooling in FM52, they must be smaller than 7 nm in size. This effective resolution limit would correspond to approximately seven M_{23}C_6 unit cells and the clustering of approximately 580 chromium atoms given the crystallography (Ref. 41) and typical composition of M_{23}C_6 (Ref. 42).

The composition of the chromium carbides along the grain boundaries in FM52 (Table 4) are in good agreement with similar compositional measurements of M_{23}C_6 made by others (Refs. 42, 43). However, this compositional data actually provides an overestimate of the metallic content (Fe, Ni, and Cr) of the precipitate. This is because the Cliff-Lorimer technique collectively groups the concentration of all elements other than Fe, Ni, and Cr into a remainder term. For the bulk composition of FM52 that remainder is $\sim 1.74 \text{ wt}\%$. However, in the M_{23}C_6 car-

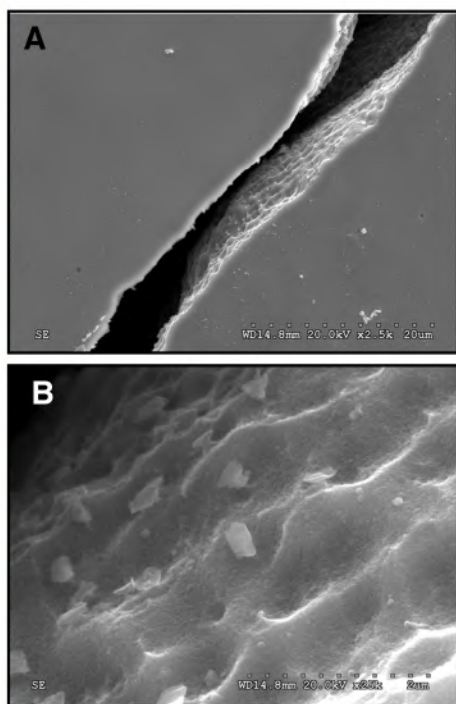


Fig. 14 — SEM fractographs taken from ductility dip crack in FM52 multipass weldment. A — Lower magnification revealing intergranular nature of crack; B — higher magnification that shows chromium-rich carbides on a wavy fracture surface.

bide the remainder term is actually ~ 5.7 wt-%. This leads to an overestimation of the metallic concentration in the carbide.

Approximately the same degree of chromium depletion is observed along the grain boundary, 25 nm away from the precipitate (21.3 ± 1.15 wt-%), as is observed directly adjacent to the precipitate at the precipitate-matrix interface (24.4 ± 1.15 wt-%) at 1600°F (871°C) on-heating, and after a 60-s hold at 1600°F on-cooling. AEM maps reveal that the grain boundary chromium depletion exists along the entire length of the boundary as seen in Figs. 8 and 10. This is a result of the nearly five order of magnitude greater chromium diffusivity along the grain boundary as compared to the matrix at 1600°F (Ref. 44). The grain boundary acts as a fast diffusion pathway for chromium in the matrix far away from the precipitate, where it is rapidly transported to the growing intergranular chromium carbide.

The asymmetric chromium depletion profiles adjacent to the precipitate-matrix interface as shown in Fig. 11 can be attributed to the growth behavior of the precipitate. As seen in Fig. 11A, the precipitate is growing from the grain boundary into the grain on the left. As the precipitate grows it preferentially depletes chromium from the left grain, thereby resulting in the asymmetric chromium depletion. Not only are the concentration profiles different on either side of the precipitate, but so is the shape of the precipitate matrix interface.

The interface the precipitate makes with the left grain is curved, while the interface with the grain on the right is straight. To minimize interfacial energy, an incoherent interface is expected to be curved. A curved incoherent interface reduces the interfacial surface area per unit volume of precipitate, thereby decreasing the interfacial energy. To the contrary, to minimize interfacial strain energy a partially coherent interface is much more likely to be straight due to the orientation relationship that the precipitate shares with the matrix. The significance of this finding to DDC will be discussed later in this paper in light of the precipitation-induced cracking hypothesis.

The precipitates and chromium depletion existent at 1600°F on-heating in FM52 are no longer present at 1600°F on-cooling. This is distinctly different than the dissolution and on-cooling precipitation behavior of A690. In A690 some intergranular chromium-rich carbides are observed at 1600°F on-cooling. These carbides form at locations where the migrated grain boundary intersects chromium-rich regions in the A690 matrix. The difference in dissolution and precipitation behavior of A690 and FM52 is related to grain boundary migration. In both alloys the peak temperature results in carbide dissolution, but in FM52 the grain boundaries remain fixed while they are found to migrate in A690. FM52's fixed grain boundaries provided a rapid diffusion path for chromium as the precipitate dissolved. This resulted in the homogenization of the near grain boundary microchemistry in FM52. This process does not happen in A690 where the boundaries migrate away from their original location, thereby leaving chromium-rich regions in the matrix where intergranular $M_{23}C_6$ precipitates were once located.

In preparation for the AEM analysis performed in this work, Desktop Spectrum Analyzer (DTSA) (Ref. 45) was utilized to estimate the minimum detectability limit (MDL) of sulfur and phosphorous. This was done using the FM52 composition and the analytical conditions of the VG 603 microscope for a collection live time of 120 s. Each DTSA spectrum was generated with the addition of Poisson's noise, which occurs with EDS analysis and degrades the MDL. Assuming a 200-nm-thick specimen, which is reasonable given the weld metal FIB specimens, the MDL for sulfur and phosphorous was below 0.1 wt-%. This limit applies not only to individual point analyses but to the summed EDS spectra shown in Fig. 12. This MDL is more than an order of magnitude lower than the ~ 5 wt-% sulfur that would have to be segregated to the grain boundary to cause em-

brittlement (Refs. 14, 15). Furthermore, this very same AEM, operated under similar conditions, was able to detect intergranular sulfur in Ni at concentrations less than 3 wt-% (Refs. 46, 47), which further validates the approach taken in the current work. Furthermore, the grain boundaries examined in the AEM were random, and thereby most likely to experience segregation of sulfur. Still, no sulfur or phosphorous segregation were detected in FM52 at 1600°F (871°C) on-heating, 1600°F on-cooling (ductility minimum), or after a 60-s hold at 1600°F on-cooling.

The summed EDS spectra from the AEM map and point analyses in Fig. 12 have a similar shape with the exception of carbon. In the summed point analyses spectrum the carbon peak has a higher ratio with the other peaks than that observed for the summed AEM maps. This may be the result of increased carbon contamination that occurred during the point analyses where the electron beam was stationary on the sample for approximately 2.5 min/measurement. During the collection of maps, the total time ("real time") the probe dwelled at each pixel was about 240 ms. The longer collection dwell time with the point analyses would be expected to result in greater carbon contamination and a larger carbon peak in the summed EDS spectra (Fig. 12B).

Fractography

A variety of intergranular fracture surfaces have been shown for ductility dip cracks formed at various temperatures (Ref. 19). However, no direct comparisons have been made between the fracture surfaces generated as part of Gleeble®-based testing and those observed in actual multipass welds. In the current work the DDC fracture surface in an FM52 multipass weld (Fig. 14) was found to be very similar to that observed in an FM52 Gleeble® hot ductility specimen fractured at 1600°F (871°C) on-cooling (Fig. 13). Both fracture surfaces have a wavy appearance and contain chromium-rich carbides. It has also been suggested that the DDC susceptibility of FM52 is at a maximum at very high temperatures ($\sim 2400^\circ\text{F}$ (1316°C)) (Ref. 21). However, the similarity between the FM52 multipass weld and the FM52 1600°F on-cooling sample (Fig. 13 and 14, respectively) indicates that the DDC mechanism was reproduced in the Gleeble®. It also supports the hypothesis that ductility dip cracks in the multipass welds occur within the same on-cooling intermediate temperature range as the Gleeble® on-cooling ductility dip (1475°–1725°F (802°–941°C)). This hypothesis is further supported when combined with the crack count data (Fig. 14 in the Part I article (Ref. 1)), which exhibits a peak in

normalized total DDC crack length over the same temperature range. A similar trend has also been shown for DDC in Invar (Ref. 3).

Interpreting DDC fracture surfaces can provide further insight into the cracking mechanism. The shape of the fracture surface features can provide insight into the loading conditions that caused fracture. For example, a hard particle located in a ductile matrix that is subjected to uniaxial tension will form microvoids with the particle located at the center of the void. If the hard particle is located on a boundary that experiences sliding, the voids will form at the precipitate/boundary interface with the particle off-center of the void. This latter type of voiding is observed along grain boundaries in both Figs. 13 and 15 ahead of the ductility dip crack tip. If the ductility dip crack were to advance, these precipitate/cavity intergranular features would be incorporated onto the DDC fracture surface. The precipitates would be present between the cavities on the fracture surface instead of being at the center of the cavities as would be the case if the loading was simply tensile.

The wavy of fracture surface morphology has been observed in wedge cracks formed during creep testing of copper (Ref. 49) and tungsten (Ref. 50) whose grain boundaries were free of precipitates. The formation of these cracks has been attributed to the formation of cavities due to GBS followed by the coalescence of these cavities to form the crack (Ref. 50). This fracture surface appearance is consistent with GBS. However, it has also been suggested that the precipitation of partially coherent intergranular $M_{23}C_6$ carbides may also result in intergranular voids that form between precipitates (Ref. 20). This may come about because the misfit at the precipitate-matrix interfaces places the matrix in compression. The region of grain boundary between the precipitates would then be placed into tension.

Strain has a significant influence on precipitation of $M_{23}C_6$ carbides in FM52. At 1600°F (871°C) on-cooling, no chromium-rich precipitates are observed in the water quench sample that was not strained (Figs. 6 and 9). However, chromium-rich precipitates are observed on the fracture surface and intergranularly in FM52 that was hot ductility tested at 1600°F on-cooling followed immediately by a water quench in Fig. 13. In this sample only 1.4 s transpired between the time the hot ductility test was initiated at 1600°F, fractured, and then water quenched to 575°F (302°C). At this lower temperature no precipitation reaction is expected to occur (Ref. 1). An increase in precipitation and coarsening of $M_{23}C_6$ has been reported in multiple austenitic alloys under a variety of straining condi-

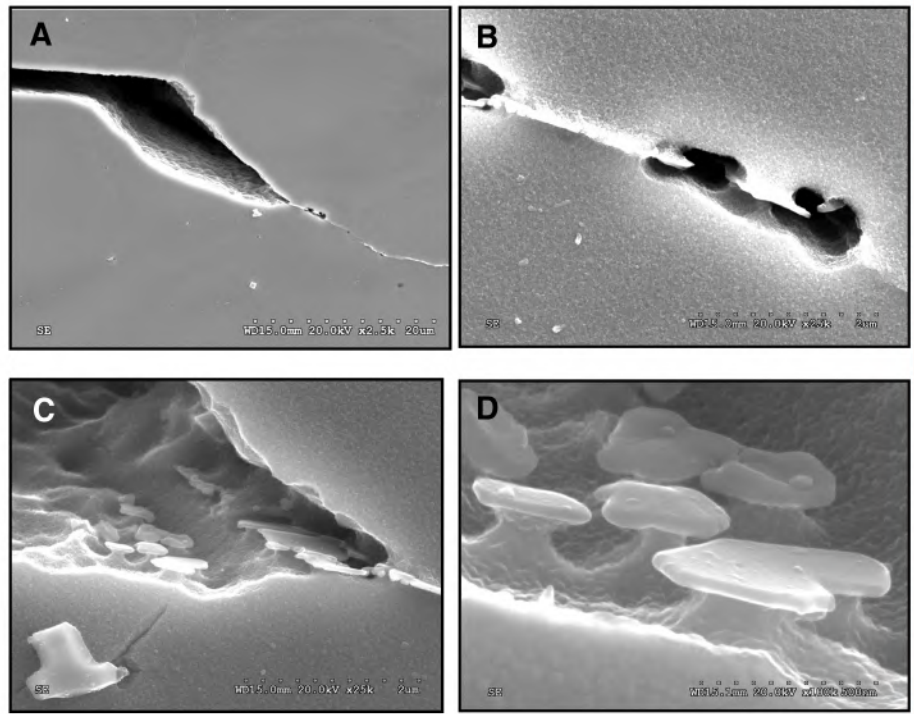


Fig. 15 — SEM fractographs from FM52 60-s hold at 1600°F hot ductility sample. A — Low magnification; B — higher magnification of voiding along intergranular precipitates; C — fracture surface; and D — chromium-rich precipitate discs along fracture surface.

tions (Refs. 51–53). In general, the kinetics of precipitation and coarsening increase with strain due to an increase in diffusivity of chromium and decrease in the thermodynamic barrier to nucleation (Ref. 51). This increase can be more than an order of magnitude greater than the precipitation kinetics of $M_{23}C_6$ in strain-free samples (Refs. 51, 53).

Predominant DDC Hypotheses in Light of Experimental Observations

P and S Embrittlement

No evidence was found that would support phosphorous and sulfur embrittlement as the cause for ductility dip cracking during the weld thermal cycle. DDC occurs in FM52 and A690 irrespective of the low sulfur and phosphorous concentrations: < 10 wt ppm S, and ≤ 50 wt ppm P in the bulk chemistry for both alloys. Therefore, it does not appear that S and P can be the cause of DDC, although increasing their concentration will most likely exacerbate DDC. Previous work performed on samples sectioned from FM52 multipass welds has revealed increases in phosphorous and sulfur concentrations at intergranular fracture surfaces (Ref. 12) and on DDC fracture surfaces (Ref. 16). As such, it is not possible to determine when the phosphorous and sulfur segregated to the boundaries.

The solubility of sulfur in nickel is at a

maximum at 2192°F (1200°C), 0.1 wt-%, then decreases to approximately 0.003 wt-% at 1179°F (Ref. 54). Although the phase boundary lines in the Ni-S system may change with the addition of chromium, iron, and other elements present in A690 and FM52, the general solubility trend can be useful to understanding the potential role of sulfur in DDC. The maximum solubility of sulfur in nickel occurs at approximately the peak temperature used for both A690 and FM52 (2422° and 2402°F, respectively (1317° and 1328°C)) in this work. If sulfur embrittlement contributes to DDC then the hot ductility should not recover with decreasing temperature, but possibly even decrease due to decreasing sulfur solubility with decreasing temperature. As the hot ductility curves show (Fig. 1), this is not the case in the alloys investigated. This may be because there is insufficient time at temperature for the sulfur to diffuse to the grain boundaries. However, the results presented in the Part I companion article demonstrates that ductility recovers and ductility dip crack length per grain boundary length decreases in FM52 with hold time at 1600°F. This is contrary to what would be expected if sulfur significantly contributed to DDC.

Precipitation-Induced Cracking (PIC)

In this work increasing intergranular precipitation before strain is applied improves ductility and decreases crack

length. This is true at all temperatures, with all alloys, and with all forms of intergranular precipitates formed within those alloys. However, the ductility minimum at 1600°F (871°C) corresponds to the same temperature at which $M_{23}C_6$ precipitates are formed when the sample is strained in both FM52 and A690. It has been proposed that the chromium concentration in the matrix can significantly affect the interfacial stresses at the $M_{23}C_6$ -matrix interface (Ref. 20). Increasing the chromium concentration in the matrix increases the precipitate-lattice misfit, thereby increasing the localized stress along the grain boundary that may, in turn, promote DDC. As the precipitate grows the matrix chromium concentration is depleted and the misfit at the interface is expected to decrease, thereby resulting in improved ductility (Ref. 20).

There are several key observations that are consistent with a PIC mechanism. First, DDC susceptibility is highest in the two alloys investigated in this work that are strong $M_{23}C_6$ carbide formers: A690 and FM52. The $M_{23}C_6$ carbide is partially coherent and some stress at the precipitate/matrix interface is expected due to lattice misfit. The second observation is that the partially coherent $M_{23}C_6$ carbides formed during straining at the ductility minimum temperature in both A690 and FM52. Consistent with the PIC hypothesis, these precipitates would be expected to have the greatest stress at the precipitate/matrix interface because they are forming into a matrix that is chromium-rich. Concurrently an external stress is being applied, which, when added to the interfacial stresses, would be expected to result in localized stresses along the grain boundary, thus producing intergranular cracking.

While the PIC hypothesis has some points of agreement with experimental observations, there are also several key findings that cannot be explained by the PIC hypothesis in its current form. The first observation is that DDC cracks also form in alloys that do not readily form $M_{23}C_6$ on-cooling. Both A600 and FM82H form incoherent intergranular precipitates (M_7C_3 and MC, respectively), and would therefore not be expected to generate stresses at the precipitate/matrix interface per the PIC hypothesis. It should be noted that $M_{23}C_6$, M_7C_3 , and TiC intergranular carbides have been observed in undeposited EN82 weld wire (Ref. 55). However, out of 140 second phases in FM82H examined by EDS in this work, only one did not contain Ti or Nb, neither of which are incorporated into $M_{23}C_6$. The one chromium-rich second phase was present after a 60-s hold at 1600°F on-cooling (Fig. 7B), where both the ductility was high and normalized ductility dip crack length was low.

The on-cooling ductility between 1725°F (941°C) and 1475°F (802°C) is significantly lower in A600 than it is on-heating. This same trend is reflected in the normalized ductility dip crack length, which is significant over the same temperature range (Ref. 1). This is the same temperature range over which the ductility dip occurs in FM52 and A690; however, FM52 and A690 have significantly fewer intergranular precipitates over this temperature range than A600 and FM82H. Intergranular precipitates can have a profound role in reducing grain boundary sliding as will be discussed below. Additionally, FM82H forms ductility dip cracks both on-heating and on-cooling. This occurs over a wide range of temperatures in FM82H from 1475°F (802°C) to 2100°F (1149°C) on-heating and from 2100°F to 1475°F on-cooling.

The second observation is that ductility dip cracks are observed in FM52 at 2100°F both on-heating and on-cooling, as was shown in the first paper (Ref. 1). This specific sample is significant for two reasons. First, the $M_{23}C_6$ carbide solvus temperature for FM52 is 2077°F (1136°C), therefore these carbides would not be expected to form while the test is being performed, although some carbides are expected to be existent in the on-heating sample because they had yet to fully dissolve. According to the PIC hypothesis the 2100°F (1149°C) on-cooling sample should be less susceptible to DDC. However, the on-cooling sample is actually more susceptible to DDC as seen in the normalized crack count data from Paper I, which is 0.6 $\mu\text{m}/\text{mm}$ for on-heating and 3.4 $\mu\text{m}/\text{mm}$ on-cooling (Ref. 1). Although this result is not expected given the PIC hypothesis, it is expected if GBS is occurring because there are fewer intergranular chromium carbides to resist GBS in the on-cooling sample, therefore its DDC susceptibility would be higher.

Lastly, the PIC hypothesis in its current form states that a decrease in chromium concentration at the precipitate-matrix interface will reduce misfit strains. This is only true when that depletion occurs along the partially coherent side of the precipitate. As shown in Fig. 11, it appears that the chromium is not depleted adjacent to the partially coherent precipitate-matrix interface, but rather along the incoherent precipitate-matrix interface that is growing into the grain on the left in Fig. 11. The observed chromium depletion will therefore have no effect on decreasing misfit strain since it is occurring along the incoherent interface. Thus, the PIC process may be a contributing factor to the observed dip in intermediate temperature ductility, but, taken alone, cannot fully explain all the observed variations in microstructure, ductility, and cracking sus-

ceptibility that occur during the weld thermal cycle.

Grain Boundary Sliding (GBS)

Grain boundary sliding is generally considered to be an operative deformation mechanism at temperatures above 0.5, the homologous temperature (T_m) (Refs. 56, 57). Strain rate is equally important to the type of failure mechanisms caused by grain boundary sliding. It has been shown that in commercially pure nickel at 700°C round intergranular cavities form when the strain rate is low (10^{-9} s^{-1}), but as the strain rate increases the type of intergranular damage transitions from round cavities to wedge-cracks, then to transgranular ductile fracture at approximately 0.1 s^{-1} (Ref. 58). Alloying additions can decrease the temperature/strain rate regime over which wedge type cracking occurs if the additions promote increases in size and volume fraction of intergranular particles and/or enhance recovery (Ref. 59). Both round cavities and wedge-cracks are a result of GBS, with wedge cracks being observed in hot ductility specimens tested as part of this program (Ref. 1). Grain boundary sliding can result in intergranular cracking when the grain interiors are stronger than the grain boundaries (Ref. 1). GBS can be reduced by an increase in intergranular particle size and volume fraction, and the formation of serrated grain boundaries (Refs. 5, 6, 58, 59). All of these grain boundary changes provide obstacles to GBS and can be thought of as increasing the friction of the grain boundary (Refs. 5, 58).

The GBS hypothesis proposes that the intermediate dip in ductility is a result of a creep-like phenomenon. Changes to the microstructure, like serrated grain boundaries and intergranular precipitates, will decrease DDC susceptibility (Ref. 60). Given these criteria, the larger, regularly spaced and homogeneously dispersed intergranular precipitates in the as-received A600 and A690 would be expected to have the lowest DDC susceptibility. This was found to be the case, as evidenced by the complete absence of DDC in either alloy during on-heating hot ductility tests (Ref. 1). It is important to note that this is the same type of intergranular carbide morphology that is prescribed for improving resistance to GBS in nickel-based superalloys (Ref. 61).

Increasing the size and volume fraction of intergranular precipitates by means of a 60-s hold at 1600°F (871°C) on-cooling or cooling from a the respective carbide solvus of the alloy decreased the DDC normalized crack length in both FM82H and FM52 (Ref. 1). The PIC hypothesis provides an explanation for the decreased crack length in FM52 but not FM82H. Ac-

cording to PIC, chromium depletion caused by $M_{23}C_6$ precipitation will decrease precipitate-matrix interfacial stress. This in turn will decrease the propensity to form ductility dip cracks once the sample is strained. However, PIC does not explain why there is a decrease in normalized DDC crack length in FM82H at 1600°F after an isothermal hold or when cooled from a lower peak temperature. The GBS hypothesis can explain both the observations for FM82H and FM52 since the increased volume fraction and size of intergranular precipitates observed in both alloys is expected to decrease grain boundary sliding and DDC susceptibility concomitantly.

The ductility dip in FM52 and A690 was preceded by the complete dissolution of $M_{23}C_6$ intergranular carbides. Similarly, dissolution of $M_{23}C_6$ intergranular carbides in SUS321H and SUS347H stainless steels resulted in increased grain boundary sliding and impaired creep rupture life (Ref. 62). $M_{23}C_6$ intergranular precipitates are considered important to improving intergranular strength in nickel based superalloys when formed as a chain of discrete globular particles (Ref. 63). The $M_{23}C_6$ intergranular precipitate volume fraction is very low in A690 and zero in FM52 at the ductility minimum temperature (1600°F on-cooling) immediately upon application of strain. When the grain boundaries are in this condition, and the driving force for dynamic recrystallization is low compared to higher temperatures, DDC susceptibility is expected to be the highest, which is the case. The on-cooling decrease in ductility and increase in ductility dip crack length in A690 can be explained in a similar manner as for A690 and FM52. The partial dissolution of intergranular carbides during the peak temperature portion of the thermal cycle rendered the grain boundaries more susceptible to sliding. However, what remains unclear is the exact role of $M_{23}C_6$ intergranular carbides in the formation of DDC since they form during the application of strain in both FM52 (Fig. 13) and A690. What is unclear is whether DDC occurs due to the dynamic formation of these intergranular precipitates or because the precipitates are not present to impede GBS at the application of strain.

Serrated boundaries are observed in both FM82H and FM52 after a 60-s hold at 1600°F (871°C) on-cooling. In FM82H, discrete NbC particles form along the grain boundary at the end of solidification. These particles prevent the boundary from migrating during post solidification cooling, which would straighten the boundary and reduce interfacial free energy. Unlike FM82H, FM52 does not contain sufficient Nb to form NbC. The serrated boundaries in FM52 (Fig. 7D) may

form in a similar way to what has been observed in AISI 316 stainless steel where an isothermal hold resulted in serration of the grain boundary followed by $M_{23}C_6$ precipitation (Refs. 64, 65). The serration of the grain boundaries was attributed to a decrease in the interfacial free energy, which offset the increase in total grain boundary area (Ref. 64). Although the serrated boundaries in FM82H and FM52 formed by different mechanisms, they both have a beneficial effect on DDC resistance. This observation is consistent with work performed on IN-792. Samples with serrated boundaries exhibited a several order of magnitude increase in time to stress rupture as compared to samples with straight boundaries (Ref. 66).

The formation of wedge-type cracks, like those observed in DDC, has also been attributed to grain boundary sliding (Refs. 58, 59, 67, 68). Grain boundary sliding is considered necessary for the formation of wedge cracks, which occur at higher strain rates than those that produce round-type cracks by diffusional processes (Refs. 58, 69). As demonstrated in Part I, the angular distribution of ductility dip cracks relative to the tensile axis was preferentially oriented in the direction of maximal shear, which is at a 45-deg angle to the tensile axis (Ref. 1). This is further evidence that GBS is playing a causal role in DDC.

Lastly, the recovery of ductility at temperatures above and below the ductility dip can be explained by the GBS hypotheses. At temperatures below the ductility minimum grain boundaries are more viscous and less likely to slide. At elevated temperatures the grain boundary sliding is impeded by dynamic recrystallization, which prevents intergranular wedge cracks from significantly growing. Thus, in summary, careful review of the data acquired in this research indicates that ductility dip cracking in these alloys is caused by GBS that may be exacerbated by highly localized stresses that develop along the matrix/ppt interface when $M_{23}C_6$ carbides form in A690 and FM52.

Comparison of Gleeble® Testing to Multipass Welds

The Gleeble® work performed in this two part series of papers was motivated by the difficulty in studying microstructural evolution and DDC susceptibility in a multipass weld. However, there are some differences in the Gleeble® testing employed herein that may affect the applicability of these results to multipass weld specimens. The first difference involves stress state. In the Gleeble®, the stress is uniaxial, whereas in multipass welds the strain state is expected to be multiaxial. Furthermore, the thin Gleeble® specimens are expected to be in a plane stress

condition, whereas multipass weld metal is most likely in a plane strain condition. Crack propagation would be expected to occur at much lower stresses in the plane strain condition. Understanding the affects of multiaxial stress state and plane stress vs. plane strain condition on DDC susceptibility is nontrivial and would require additional research. Specifically, how these two affect GBS and PIC in these alloys. However, the results from uniaxial Gleeble® hot ductility tests in this work provide a useful step in understanding this complex phenomenon.

The second difference between Gleeble® testing and multipass welds is the strain rate. In the Gleeble® testing the strain rate ($\sim 1s^{-1}$) is higher than would be expected in a multipass weld. However, it was found that this higher strain rate actually resulted in a more aggressive testing condition for screening the DDC susceptibility of alloys (Ref. 1). Additionally, in the Gleeble® test the samples were strained until they fractured into two pieces. This high level of strain is never encountered in multipass welds. This difference helps to explain why some ductility dip cracks were observed in FM82H Gleeble® specimens tested in this work, but multiple heats of FM82H were found to be free of DDC in multipass welds (Refs. 20, 22). With respect to strain, the Gleeble® testing performed in this work is more adverse than would be experienced in multipass welds.

In the Gleeble® tests performed as part of this work the material was only subjected to one thermal cycle, and the strain was not applied concurrently with cooling or heating. This is the third difference between Gleeble® and multipass welds. In multipass welds the sample is strained and heated or cooled at the same time over the course of multiple thermal cycles. This may result in greater precipitation of second phases that promote DDC.

Lastly, in multipass welds the peak temperature is higher than what was evaluated in the Gleeble® tests performed in this work. Higher peak temperatures will result in dissolution of NbC carbides, thereby freeing up carbon that can potentially form intergranular $M_{23}C_6$ precipitates. These precipitates may prove detrimental to DDC resistance, which requires further research.

Conclusions

The DDC susceptibility of A600, A690, FM82H, and FM52 has been determined using Gleeble® hot ductility testing and correlated to the microstructural evolution of these alloys during the first weld thermal cycle. The following conclusions can be drawn from this research:

1. No evidence of sulfur or phospho-

rous segregation was found in FM52 in water-quenched samples from the ductility minimum temperature, 1600°F (871°C) on-cooling, 1600°F on-heating, or after a 60-s isothermal hold at 1600°F. Based on this sulfur and phosphorous embrittlement does not cause DDC during the first weld thermal cycle, although they will most likely exacerbate DDC if present at higher concentration.

2. Within the ranges tested, grain size does not play a role in DDC for the alloys considered. The grain size of FM52 was 2.5 times greater than that of A690, but they both experienced a ductility minimum at 1600°F (871°C) on-cooling. Conversely, the grain sizes of A600 and A690 at the same temperature were the same, within experimental error, but there was no ductility dip in A600.

3. Dissolution of intergranular carbides was observed in A600, A690, and FM52 during the peak temperature portion of the thermal cycle. This dissolution preceded a reduction in ductility and increased susceptibility to DDC over an intermediate temperature range [1725°–1475°F (941°–802°C) on-cooling] in all three alloys. This decrease in intergranular carbide size and volume fraction appears to promote grain boundary sliding.

4. Cooling FM82H and FM52 from peak temperatures that correspond to their carbide solvus resulted in increased intergranular carbide coverage. Similarly, an isothermal hold at 1600°F (871°C) (the ductility minimum for A690 and FM52) resulted in more intergranular carbides in both FM82H and FM52. Increased intergranular carbide coverage reduces DDC susceptibility regardless of carbide type. This increase in intergranular carbide size and volume fraction would promote grain boundary sliding.

5. Ductility dip cracking in these alloys appears to be caused by GBS that may be exacerbated by highly localized stresses. These stresses may develop along the matrix/precipitate interface when $M_{23}C_6$ carbides form in the same time/temperature regime as the hot ductility test.

Acknowledgments

This work was funded by a Naval Nuclear Propulsion Program Fellowship sponsored by Naval Reactors Division of the U.S. Department of Energy. The authors would like to thank Dr. George Young Jr. and Tom Capobianco of Lockheed Martin for their assistance in this work. The authors also appreciate the advice of Dr. Chris Kiely, Dave Ackland, and Bill Mushock of Lehigh University with regards to electron microscopy. Additionally, Noecker thanks Dr. Tom Lienert of Los Alamos National Laboratory for his continuing interest in this work and helpful discussions.

References

- Noecker II, F. F., and DuPont, J. N. 2009. Metallurgical investigation into ductility dip cracking in Ni-based alloys: Part I. *Welding Journal* 88(1): 7-s to 20-s.
- Rhines, F. N., and Wray, P. J. 1961. Investigation of the intermediate-temperature ductility minimum in metals. *Am. Soc. Metals, Trans. Quartz* 54(2): 117–128.
- Zhang, Y. C., Nakagawa, H., and Matsuda, F. 1985. Weldability of Fe-36%Ni alloy report III: Dynamic observation of reheat hot crack and evaluation of hot ductility of reheated weld metal. *Trans. JWRI* 14(1): 107–114.
- Nissley, N. E., and Lippold, J. C. 2003. Development of the strain-to-fracture test: A new test has been established for evaluating ductility dip cracking susceptibility in austenitic alloys. *Welding Journal* 82(12): 355-s to 364-s.
- Raj, R., and Ashby, M. F. 1971. On grain boundary sliding and diffusional creep. *Metallurgical Transactions* 2(4): 1113–1127.
- Raj, R., and Ashby, M. F. 1972. Grain boundary sliding, and the effects of particles on its rate. *Metallurgical Transactions* 3(7): 1937–1942.
- Mulford, R. A. 1983. Grain-boundary embrittlement of nickel and nickel alloys. *Treatise on Materials Science and Technology* 25: 1–19.
- Lozinskiy, M. G., Volkogon, G. M., and Pertsovskiy, N. Z. 1967. Investigation of the influence of zirconium additions on the ductility and deformation structure of nickel over a wide temperature range. *Russian Metallurgy* 5: 65–72.
- Nishimoto, K., Mori, H., and Hirata, H. 2001. Effect of grain boundary segregation of sulphur on reheat cracking susceptibility in multipass weld metal of Fe-36%Ni alloy. *Today and Tomorrow in Science and Technology of Welding and Joining, Proceedings of the 7th Japanese Welding Society International Symposium*. T. Ohji, pp. 827–832. Japan Welding Society.
- Matsuda, F., Nakagawa, H., Minehisa, S., Sakabata, N., Ejima, A., and Nohara, K. 1984. Weldability of Fe-36% Ni alloy report II: Effect of chemical composition on reheated hot cracking in weld metal. *Trans. JWRI* 13(2): 69–75.
- Ogawa, T. 1986. Weldability of Invar and its large-diameter pipe. *Welding Journal* 65(8): 213-s to 226-s.
- Nishimoto, K., Saida, K., Okauchi, H., and Ohta, K. 2006. Microcracking in multipass weld metal of Alloy 690. Part 2: Microcracking mechanism in reheated weld metal. *Science and Technology of Welding and Joining* 11(4): 462–470.
- Nishimoto, K., Saida, K., Okauchi, H., and Ohta, K. 2006. Microcracking in multipass weld metal of Alloy 690. Part 3: Prevention of microcracking in reheated weld metal by addition of La to filler metal. *Science and Technology of Welding and Joining* 11(4): 471–479.
- Heuer, J. K., Okamoto, P. R., Lam, N. Q., and Stubbins, J. F. 2002. Disorder-induced melting in nickel: Implication to intergranular sulfur embrittlement. *Journal of Nuclear Materials* 301(2-3): 129–141.
- Yamaguchi, M., Shiga, M., and Kaburaki, H. 2005. Grain boundary decohesion by impurity segregation in a nickel-sulfur system. *Science* 307(5708): 393–397.
- Capobianco, T. E., and Hanson, M. E. 2006. Auger spectroscopy results from ductility dip cracks opened under ultra-high vacuum. *Proceedings of the 7th International Trends in Welding Research Conference*. Eds. S. A. David, et al., pp. 767–772. ASM International.
- Zhang, Y. C., Nakagawa, H., and Matsuda, F. 1985. Weldability of Fe-36%Ni alloy report VI: Further investigation on mechanism of reheat hot cracking in weld metal. *Trans. JWRI* 14(2): 125–134.
- Matsuda, F., Nakagawa, H., Ogata, S., and Katayama, S. 1978. Studies on the fractography of welded zones. Report 3 - Fractographic investigation on solidification crack in the vareststraint test of fully austenitic stainless steel. *Transactions of JWRI* 7(1): 59–70.
- Collins, M. G., Ramirez, A. J., and Lippold, J. C. 2003. An investigation of ductility dip cracking in nickel-based weld metals. Part II: Fracture behavior and fracture surface morphology are related to microstructure, composition, and temperature. *Welding Journal* 82(12): 348-s to 354-s.
- Young, G. A., Capobianco, T. E., Penik, M. A., Morris, B. W., and McGee, J. J. 2007. The mechanism of ductility dip cracking in nickel-chromium alloys. *Welding Journal* 87(2): 31-s to 43-s.
- Nishimoto, K., Saida, K., and Okauchi, H. 2006. Microcracking in multipass weld metal of Alloy 690. Part 1: Microcracking susceptibility in reheated weld metal. *Science and Technology of Welding and Joining* 11(4): 455–461.
- Young, G. A., Capobianco, T. E., and Etien, R. 2007. Development of a highly weldable and corrosion resistant Ni-Cr filler metal. *Degradation 2007: 13th International Conference on Environmental Degradation in Nuclear Power Systems*. Eds. T. R. Allen, J. T. Busby, and P. T. King, compact disc (CD). Canadian Nuclear Society.
- Collins, M. G., and Lippold, J. C. 2003. An investigation of ductility dip cracking in nickel-based filler materials. Part I: The strain-to-fracture test has been used to develop temperature-strain relationships for ductility dip cracking. *Welding Journal* 82(10): 288-s to 295-s.
- Collins, M. G., Ramirez, A. J., and Lippold, J. C. 2004. An investigation of ductility-dip cracking in nickel-based weld metals. Part III: The characteristics of weld-metal grain boundaries associated with elevated-temperature fracture are investigated. *Welding Journal* 83(2): 39-s to 49-s.
- Dave, V. R., Cola, M. J., Kumar, M., Schwartz, A. J., and Hussen, G. N. A. 2004. Grain boundary character in Alloy 690 and ductility-dip cracking susceptibility. *Welding Journal* 83(1): 1-s to 5-s.
- Nissley, N. E. 2006. Intermediate temperature grain boundary embrittlement in nickel-base weld metals. PhD diss., Columbus, Ohio, The Ohio State University. http://www.ohiolink.edu/ed/view.cgi?acc_num=osu1156949345
- ASTM E112-96, *Standard Test Methods for Determining Average Grain Size*. 1996. Conshohocken, Pa.: American Society for Testing and Materials.
- Lim, Y. S., Kim, J. S., Kim, H. P., and Cho, H. D. 2004. The effect of grain boundary misorientation on the intergranular $M_{23}C_6$ carbide precipitation in thermally treated Alloy 690. *Journal of Nuclear Materials* 335(1): 108–114.
- Hong, H. U., Rho, B. S., and Nam, S. W. 2001. Correlation of the $M_{23}C_6$ precipitation morphology with grain boundary characteris-

tics in austenitic stainless steel. *Materials Science & Engineering A* A318(1-2): 285-292.

30. Bouchet, D., and Priester, L. 1986. Intergranular segregation and crystallographic parameters of grain boundaries in nickel-sulfur system. *Scripta Metallurgica* 20(7): 961-966.

31. Cliff, G., and Lorimer, G. W. 1975. The quantitative analysis of thin specimens. *Journal of Microscopy* 103(2): 203-207.

32. Williams, D. B., and Carter, C. B. 1996. *Quantitative X-ray Microanalysis. Transmission Electron Microscopy IV: Spectrometry*. New York: Plenum, 599-620.

33. Inconel Alloy 600. Special Metals, 2007. p. 16. (<http://www.specialmetals.com/documents/Inconel%20alloy%20600.pdf>)

34. Airey, G. P. 1980. Microstructural aspects of the thermal treatment of Inconel Alloy 600. *Metallography* 13(1): 21-41.

35. Inconel Alloy 690. Special Metals, 2007. p. 8. (<http://www.specialmetals.com/documents/Inconel%20alloy%20690.pdf>)

36. Ramirez, A. J., and Lippold, J. C. 2004. High temperature behavior of Ni-base weld metal. Part I: Ductility and microstructural characterization. *Materials Science & Engineering A* A380(1-2): 259-271.

37. Williams, D. B., and Carter, C. B. 1996. *Quantitative X-ray Microanalysis. Transmission Electron Microscopy IV: Spectrometry*. New York: Plenum, 623-635.

38. Isoard, V., and Rack, H. J. 1997. High temperature grain growth in Inconel 690. *THERMEC '97, International Conference on Thermomechanical Processing of Steels and Other Materials, 2nd*. Eds. T. Chandra, T. Sakai, pp. 1737-1744. TMS.

39. Lee, J. A., Lee, J. H., Kim, J. J., and Chai, Y. S. 2005. Effects of heat treatment condition on the microstructure evolution of Inconel 690. *Key Engineering Materials* 297-300(1): 458-462.

40. Lim, Y. S., Hwang, S. S., Suh, J. H., and Kim, J. S. 2001. Grain growth and intergranular carbide precipitation in nickel-base Alloy 690. *Recrystallization and Grain Growth, Proceedings of the 1st Joint International Conference*. Eds. G. Gottstein and D. A. Molodov, pp. 389-394. Springer-Verlag.

41. Yakel, H. L. 1987. Atom distributions in tau-carbide phases: Iron and chromium distributions in chromium iron carbide ($\text{Cr}_{23-x}\text{Fe}_x\text{C}_6$ with $x = 0, 0.74, 1.70, 4.13$ and 7.36). *Acta Crystallographica, Section B: Structural Science* B43(3): 230-238.

42. Angelili, T. M., and Was, G. S. 1990. Behavior of grain boundary chemistry and precipitates upon thermal treatment of controlled purity Alloy 690. *Metallurgical Transactions A* 21A(8): 2097-2107.

43. Thuvander, M., and Stiller, K. 2000. Microstructure of a boron containing high purity nickel-based Alloy 690. *Materials Science & Engineering A* A281(1-2): 96-103.

44. Pruthi, D. D., Anand, M. S., and Agarwala, R. P. 1977. Diffusion of chromium in Inconel-600. *Journal of Nuclear Materials* 64(1-2): 206-210.

45. Fiori, C., Swyt-Thomas, C., and Myklebust, B. *Desktop Spectrum Analyzer*. National Institute of Standards and Technology. <http://www.cstl.nist.gov/div837/Division/outputs/D TSA/DTSA.htm>

46. Keast, V. J., and Williams, D. B. 2001. Grain boundary chemistry. *Current Opinion in Solid State & Materials Science* 5(1): 23-30.

47. Keast, V. J., and Williams, D. B. 2000.

Quantification of boundary segregation in the analytical electron microscope. *Journal of Microscopy* 199(1): 45-55.

48. Hull, D. 1999. *Fractography*. Cambridge, UK: Cambridge University Press, 235-244.

49. Fields, R. J., and Ashby, M. F. 1980. Observation of wedge cavities in the S.E.M. *Scripta Metallurgica* 14(7): 791-795.

50. Stiegler, J. O., Farrell, K., Loh, B. T. M., and McCoy, H. E. 1967. Nature of creep cavities in tungsten. *ASM Transactions Quarterly* 60(3): 494-503.

51. Advani, A. H., Murr, L. E., Atteridge, D. G., and Chelakara, R. 1991. Mechanisms of deformation-induced grain boundary chromium depletion (sensitization) development in type 316 stainless steels. *Metallurgical Transactions A* 22A(12): 2917-2934.

52. Iwashita, C. H., and Wei, R. P. 2000. Coarsening of grain boundary carbides in a nickel-based ternary alloy during creep. *Acta Materialia* 48(12): 3145-3156.

53. Trillo, E. A., Beltran, R., Maldonado, J. G., Romero, R. J., Murr, L. E., Fisher, W. W., and Advani, A. H. 1995. Combined effects of deformation (strain and strain state), grain size, and carbon content on carbide precipitation and corrosion sensitization in 304 stainless steel. *Materials Characterization* 35(2): 99-112.

54. Brigham, R. J., Neumayer, H., and Kirkaldy, J. S. 1970. Solubility limit for sulfur in nickel between 637° and 1400°. *Canadian Metallurgical Quarterly* 9(4): 525-529.

55. Briant, C. L., and Hall, E. L. 1987. The microstructural causes of intergranular corrosion of Alloys 82 and 182. *Corrosion* 43(9): 539-548.

56. Dieter, G. E. 1986. *Mechanical Metallurgy*. Boston, Mass.: McGraw Hill, 185-188.

57. Hertzberg, R. W. 1996. *Deformation and Fracture Mechanics of Engineering Materials*. New York, N.Y.: John Wiley and Sons, Inc., 157-207.

58. Gandhi, C., and Raj, R. 1981. An upper bound on strain rate for wedge type fracture in nickel during creep. *Metallurgical Transactions A* 12A(3): 515-520.

59. Raj, R. 1981. Development of a processing map for use in warm-forming and hot-forming processes. *Metallurgical Transactions A* 12(6): 1089-1097.

60. Ramirez, A. J., and Lippold, J. C. 2004. High temperature behavior of Ni-base weld metal. Part II: Insight into the mechanism for ductility dip cracking. *Materials Science & Engineering A* A380(1-2): 245-258.

61. Donachie, M. J., and Donachie, S. J. 1998. Properties and microstructure of superalloys. In *Metals Handbook Desk Edition*. Ed. J. R. Davis, pp. 394-414. Materials Park, Ohio: ASM International.

62. Tanaka, H., Murata, M., Abe, F., and Yagi, K. 1997. The effect of carbide distributions on long-term creep rupture strength of SUS321H and SUS347H stainless steels. *Materials Science & Engineering A* A234-236: 1049-1052.

63. Vander Voort, G. F., Lucas, G. M., and Manilova, E. P. 2004. Metallography and microstructures of heat-resistant alloys. In *ASM Handbook Volume 9: Metallography and Microstructures*. Ed. G. F. Vander Voort, pp. 820-859. Materials Park, Ohio: ASM International.

64. Hong, H. U., and Nam, S. W. 2001. Crystallographic investigations on the serrated grain

boundaries in an AISI 316 stainless steel. *Zeitschrift fuer Metallkunde* 92(12): 1331-1334.

65. Hong, H. U., and Nam, S. W. 2002. The occurrence of grain boundary serration and its effect on the M_{23}C_6 carbide characteristics in an AISI 316 stainless steel. *Materials Science & Engineering A* A332(1-2): 255-261.

66. Larson, J. M., and Floreen, S. 1977. Metallurgical factors affecting the crack growth resistance of a superalloy. *Metallurgical Transactions A* 8A(1): 51-55.

67. Shapiro, E., and Dieter, G. E. 1970. High temperature-high strain rate fracture of Inconel 600. *Metallurgical Transactions* 1: 1711-1719.

68. Shapiro, E., and Dieter, G. E. 1971. Fracture and ductility in hot torsion of nickel. *Metallurgical Transactions* 2(5): 1385-1391.

69. Waddington, J. S. 1968. Conditions affecting the mechanism of fracture at high temperatures. *Philosophical Magazine* 17(145): 51-59.

REPRINTS

REPRINTS

To order custom reprints of 100 or more of articles in

Welding Journal, call FosteReprints at (219) 879-8366 or (800) 382-0808.

Request for quotes can be faxed to (219) 874-2849.

You can e-mail FosteReprints at sales@fostereprints.com.